Lamin C Counteracts Glucose Intolerance in Aging, Obesity, and Diabetes Through β-Cell Adaptation

Marion de Toledo, Isabel C. Lopez-Mejia, Patricia Cavelier, Marine Pratlong, Célia Barrachina, Xavier Gromada, Jean-Sébastien Annicotte, Jamal Tazi, Carine Chavey

▶ **To cite this version:**

Marion de Toledo, Isabel C. Lopez-Mejia, Patricia Cavelier, Marine Pratlong, Célia Barrachina, et al.. Lamin C Counteracts Glucose Intolerance in Aging, Obesity, and Diabetes Through β-Cell Adaptation. Diabetes, 2020, 69 (4), pp.647-660. 10.2337/db19-0377 . hal-03065207

HAL Id: hal-03065207
https://hal.science/hal-03065207

Submitted on 14 Dec 2020

HAL is a multi-disciplinary open access archive for the deposit and dissemination of scientific research documents, whether they are published or not. The documents may come from teaching and research institutions in France or abroad, or from public or private research centers.

L'archive ouverte pluridisciplinaire **HAL**, est destinée au dépôt et à la diffusion de documents scientifiques de niveau recherche, publiés ou non, émanant des établissements d'enseignement et de recherche français ou étrangers, des laboratoires publics ou privés.

Lamin C counteracts glucose intolerance in aging, obesity and diabetes through β-cell adaptation

Running title: Lamin C involvement in β-cell adaptation

Marion de Toledo[1]*, Isabel C. Lopez-Mejia[2], Patricia Cavelier[1], Marine Pratlong[3], Célia Barrachina[3], Xavier Gromada[4], Jean-Sébastien Annicotte[4#], Jamal Tazi[1#*] & Carine Chavey[1#*].

[1]Institut de Génétique Moléculaire de Montpellier, University of Montpellier, CNRS, Montpellier, France

[2]Center for Integrative Genomics, University of Lausanne, Lausanne, Switzerland

[3]MGX, Biocampus Montpellier, CNRS, INSERM, University of Montpellier, Montpellier, France

[4]Univ. Lille, CNRS, CHU Lille, Institut Pasteur de Lille, UMR 8199 - EGID, F-59000 Lille, France

[#]Authors share co-authorship

* Correspondence: Marion de Toledo, PhD, Institut de Génétique Moléculaire de Montpellier, University of Montpellier, CNRS, Montpellier, France. e-mail: marion.detoledo@igmm.cnrs.fr; Carine Chavey, PhD, Institut de Génétique Moléculaire de Montpellier, University of Montpellier, CNRS, Montpellier, France. e-mail: carine.chavey@igmm.cnrs.fr; Jamal Tazi, Professor, Institut de Génétique Moléculaire de Montpellier, University of Montpellier, CNRS, Montpellier, France. e-mail: jamal.tazi@igmm.cnrs.fr;

Total word count : 5293 words

Number of figure/table: 6 figures, 6 supplemental datas, 2 supplemental tables

Diabetes Publish Ahead of Print, published online January 31, 2020

Abstract

Aging-dependent changes in tissue function are associated with the development of metabolic diseases. However, the molecular connections linking aging, obesity and diabetes remain unclear. Lamin A, lamin C and progerin, products of the *Lmna* gene, have antagonistic functions on energy metabolism and lifespan. Lamin C, albeit promoting obesity, increases lifespan suggesting that this isoform is crucial for maintaining healthy conditions under metabolic stresses. Since β-cell loss during obesity or aging leads to diabetes, we investigated the contribution of lamin C to β-cell function in physiopathological conditions. We demonstrate that aged lamin C-only expressing mice (*Lmna*$^{LCS/LCS}$) become obese but remain glucose tolerant, due to adaptive mechanisms including increased β-cell mass and insulin secretion. Triggering diabetes in young mice revealed that *Lmna*$^{LCS/LCS}$ animals normalize their fasting glycemia by both increasing insulin secretion and regenerating β-cells. Genome-wide analyses combined to functional analyses revealed an increase of mitochondrial biogenesis and global translational rate in *Lmna*$^{LCS/LCS}$ islets, two major processes involved in insulin secretion. Altogether, our results demonstrate for the first time, that the sole expression of lamin C protects from glucose intolerance through a β-cell adaptive transcriptional program during metabolic stresses highlighting *Lmna* gene processing as a new therapeutic target for diabetes treatment.

Introduction

Lamin A, lamin C and progerin proteins, produced by alternative RNA processing of the *Lmna* gene, are intermediate filaments that bridge peripheral heterochromatin to the nuclear envelope (1), thus participating in the maintenance of chromatin architecture (2,3) and in transcriptional regulation (4). Mutations in the *Lmna* gene result in laminopathies, including progeria, which lead to metabolic abnormalities such as lipodystrophy, hypertriglyceridemia, insulin resistance and metabolic syndrome, thus suggesting an important role for A-type lamins in the regulation of glucose and lipid metabolism (5). Comparing Knock-in mice expressing all three lamin isoforms (lamin A, lamin C and progerin) or exclusively lamin C isoform ($Lmna^{LCS/LCS}$), we previously reported antagonistic functions of *Lmna* isoforms in energy expenditure and lifespan, pointing out a key function for this gene in the control of energy homeostasis (6). Despite showing increased body weight, $Lmna^{LCS/LCS}$ have an unexpectedly increased lifespan suggesting a role for lamin C in improving metabolic health during aging.

Pancreatic β cells play a critical role in maintaining glucose homeostasis through the secretion of insulin, and their dysfunction results in diabetes. Whereas type 1 diabetes (T1D) is an autoimmune disease that results from the destruction of β-cells, type 2 diabetes (T2D) is due to energy imbalance and is characterized by impaired peripheral insulin sensitivity followed by defects in insulin secretion. The common hallmark of T1D and T2D is an inadequate supply of functional insulin-producing β-cells, leading to the dysregulation of glucose metabolism and associated metabolic complications (7). The restoration of normal β-cell mass and function has therefore become of great interest for the generation of novel anti-diabetic drugs. In this context, β-cell regeneration has been extensively explored in mice and humans. However, the mechanisms involved in the functional plasticity required for the regeneration of β-cell mass remain poorly understood (7, 8).

Although recent reports highlighted that *Lmna* isoforms are involved in the structure and function of the exocrine pancreas (9), their contribution to the endocrine pancreas and, more particularly, in insulin-producing β-cells remain to be investigated. We hypothesized that lamin C might contribute to maintain adequate glucose homeostasis during aging through a role on pancreatic β-cell plasticity or regeneration. Using a comprehensive analysis of the metabolic phenotype of *Lmna*$^{LCS/LCS}$ mice using different models related to β-cell failure (*i.e.* aging, STZ-induced diabetes and obesity-induced diabetes), we demonstrate that exclusive lamin C expression favors β-cell mass, insulin production and insulin secretion in conditions where dual expression of lamin A and lamin C from the *Lmna* gene are accompanied by abnormal glucose homeostasis. This adaptive effect on β-cell mass and function is associated with an increase in mitochondrial activity and of global translation rates, providing a molecular link between lamin C and β-cell fitness during aging. Using a model of T2D (diet-induced obesity, DIO), we report that *Lmna*$^{LCS/LCS}$ mice enhance insulin secretion to adapt to DIO and to maintain normoglycemia. Finally, in streptozotocin-induced diabetes mice β-cell failure was rescued in *Lmna*$^{LCS/LCS}$ through increased regeneration of β-cells. Altogether, our findings demonstrate that the exclusive expression of lamin C improves β-cell function and mass during metabolic stress and suggest that the manipulation of *Lmna* isoforms can be targeted to counteract diabetes.

Research Design and Methods

Animal experiments and ethics statement

Lmna$^{LCS/LCS}$ Knock-In mice were bred onto C57BL/6J background as described (10). All animal procedures were conducted in accordance with the French national animal care guidelines. Mice were maintained in pathogen-free conditions in our animal facility (E34-172-16). Mice were housed under a 12-h light/dark cycle and given an *ad libitum* regular chow diet (A04; Safe). All experiments were conducted by authorized personnel (agreements MDT34-433; CC-I-34UnivMontp-f1-12) and approved by the Ethics Committee of the Languedoc-Roussillon region Montpellier (CEEA-LR-12003). Male mice were used for *in vivo* experiments and isolated islets were prepared from male or female mice.

Histology and immunohistochemistry

Pancreas sections (4µm) were deparaffinized, rehydrated, stained with hematoxylin and eosin (HE) and visualized with a Nanozoomer. Islets diameter were measured using NDP View software.

For immunohistochemistry, rehydrated sections were incubated in citrate buffer at 95°C for 30min. After blocking, sections were incubated in primary antibodies (see table 2) overnight at 4°C and were detected using appropriate secondary antibodies. Nuclei were counterstained with Hoechst® 33342.

Metabolic analysis and generation of diabetic mouse models

For IPGTT, 18 h-fasted mice were injected intraperitoneally with glucose (1.7g/kg), and glycemia was measured using a blood glucometer (Roche). Insulin levels were quantified using

Mouse Ultrasensitive Insulin ELISAs (ALPCO). To induce T2D, 12-week-old mice had unrestricted acces to a HFD (ResearchDiet) for 25 weeks. To induce acute β-cell loss, 13 weeks old mice were injected i.p. with a single high dose (200mg/kg) of streptozotocin (Sigma-Aldrich) dissolved in 0.1M sodium citrate buffer (pH4.4).

Pancreatic islet Isolation and Glucose-stimulated insulin secretion

Mouse islets were isolated by type V collagenase digestion (Sigma) of pancreata. After separation in a density gradient medium (Histopaque®-1119, Sigma), islets were handpicked. They were then cultured for 18–20h at 37°C in a 95% air-5% CO_2 atmosphere in RPMI-1640 (ThermoFisher) containing 10% FCS and 100 µg/ml penicillin-streptomycin.

To evaluate insulin secretion, 3 replicates of 5 islets were preincubated for 1h at 37°C in KRB buffer. After low (3mM) or high (20mM) glucose stimulation, secreted insulin and total insulin cell content were measured. Data are expressed as a ratio of secreted insulin/total insulin content.

Total pancreatic insulin and glucagon content

Pancreata were lysed in 2ml Acid/Ethanol lysis buffer and incubated O/N at 4°C. After neutralization with 10% of 1M Na2CO3, total insulin and glucagon content were measured by ELISA (Mouse Ultrasensitive Insulin elisa-ALPCO, Mercodia Glucagon ELISA - 10 µL).

RT-qPCR analysis and mitochondrial DNA quantification

Total RNA was extracted from isolated islets using TRIzol (Life Technologies, USA).. Samples were quantified with a NanoDrop ND-1000. 1.5 µg RNA were then converted to cDNA

with the Maxima First Strand cDNA Synthesis Kit (#K1642, Thermo Scientific). Gene expression was normalized to cyclophillin and TBP.

For mitochondrial DNA quantification, islets were digested using proteinaseK. qPCR analysis was performed with primers specific for mitochondrial genes (*mtND5*, *mt16s*) and normalized to nuclear genes (*LN11*, *HK2*).

qPCR was performed with a LightCycler® 480 and LightCycler® 480 SYBR GreenI Master (Roche). Primer sequences are provided in Supplemental Table 1.

Ultrastructural transmission electron microscopy

After isolation, 150 islets were immersed in a solution of 2.5% glutaraldehyde. After dehydration, samples were embedded in EmBed812. 70nm sections were counterstained with uranyl acetate and observed on a Hitachi-7100 microscope.

Seahorse experiments and metabolic flux analysis

Oxygen consumption rate (OCR) was measured in 96-well plates using a XFe96-Seahorse (Agilent). Briefly, 25 islets/well were plated in poly-D-lysine-coated wells in XF-assay medium containing 3mM glucose, 1mM sodium pyruvate and 1mM glutamine (pH7.4) for 1 h at 37°C without CO_2. OCRs were monitored in response to glucose (20mM), oligomycin (2µM), FCCP (1µM) and rotenone (0.5µM). OCRs measurements were normalized by total DNA level using a Qubit dsDNA HS assay kit (LifeTechnologies).

Incorporation of ^{35}S-Met/Cys into isolated islets

Seventy isolated islets were incubated in Met/Cys-depleted RPMI medium (Sigma) for 30min and then supplemented with 50µCi ^{35}S-Met/Cys EasyTag Express (PerkenElmer) for

30min at 37°C. Islets were lysed in RIPA buffer. 10µg of total protein were size-fractionated on 4-12% gradient SDS-PAGE. The gel was dried and quantified using a PhosphoImager (GE-Healthcare).

Flow cytometry

Islets dissociated with 0.05% Trypsine-0.5 mM EDTA were fixed with 1% PFA and permeabilised with 0.05% Triton X-100. After blocking, cells were incubated anti-insulin antibody, washed, reacted with a FITC-conjugated antibody and analyzed by FACSCANTO II (Becton Dickinson).

RNA isolation, RNA-seq, RRBS, ATAC-seq and data analysis

Total RNA was extracted using TRIzol and quantified on Qubit (Life Technologies). RNA quality was verified using RNA pico-chips on a 2100-Bioanalyzer (Agilent). Total DNA was purified using MasterPure™ Complete DNA (Illumina). Libraries for RNA-seq and RRBS were prepared and sequenced by the MGX sequencing platform in Montpellier (France).

For ATAC-seq analyses, islets were cryopreserved in 50%FCS, 40%RPMI, 10%DMSO and processed by ActiveMotif.

All data are deposited in GEO-NCBI under accession number GSE122361.

Statistical analysis

Results were expressed as the mean ± SEM. Statistical comparison were made using student's t-test. Statistically significant diffrencies are indicated as *$p<0.05$, **$p< 0.01$, ***$p< 0.001$, ****$p< 0.0001$

A detailed description of the all procedures and bioinformatic analyses can be found in Supplementary Methods.

Data and Resource Availability

The resources generated during and/or analyzed during the current study are available from the corresponding authors on reasonable request. The genome wide datas generated and/or analyzed during the current study are deposited in GEO-NCBI under accession number GSE122361.

Results

Increased obesity in aged *Lmna*$^{LCS/LCS}$ mice is associated to improved glucose tolerance

To evaluate whether lamin C regulates β-cell function, we evaluated glucose homeostasis in *Lmna*$^{LCS/LCS}$ mice (6). Initially designed to generate a mouse model of progeria, the c.1827C>T;p.G609G point mutation was introduced into a floxed neo cassette (Supplemental data 1A). This cassette was inserted in intron-10 of the *Lmna* gene, downstream of the polyadenylation site of lamin C, thus preventing the formation of prelamin A transcripts by blocking lamin A-specific splicing (10). The conditional mutant allele (*Lmna*^{LCS}) resulted in the exclusive expression of lamin C. This was confirmed by comparing its levels in brain, liver, pancreas and muscle from *Lmna*$^{+/+}$ (wild type, WT) and *Lmna*$^{LCS/LCS}$ mice (Supplemental data 1B). We observed increased expression of lamin C in *Lmna*$^{LCS/LCS}$ mice compared to WT in most tissues except in the brain, where the lamin C/lamin A ratio is already high even in WT mice, as previously shown (11).

With the experimental *Lmna*$^{LCS/LCS}$ model established, we then investigated the metabolic phenotype of these mice. The *Lmna*$^{LCS/LCS}$ mice gained more weight than control mice as they aged (Fig 1A). This increase in boby weight is mainly due to an increase in white adipose tissue without any further change in body composition as shown in our previous study (6). Body weight and fasting glucose levels in *Lmna*$^{+/+}$ and *Lmna*$^{LCS/LCS}$ mice were similar until 25 weeks of age (Fig 1A-B). Interestingly, the significant increase in body weight was observed from 30 weeks of age in *Lmna*$^{LCS/LCS}$ mice, but was even more pronounced at 75 weeks of age. The following aging experiments are thus conducted by comparing “young” (25 weeks old) to “old” animals (75 weeks old). We observed a significant increase in fasting glycemia in control mice as they aged (Fig 1B). Interestingly *Lmna*$^{LCS/LCS}$ mice remained normoglycemic, although an increased body weight is typically associated with hyperglycemia. These findings prompted us

to analyze glucose homeostasis in aged *Lmna*$^{LCS/LCS}$ mice. Glucose clearance was similar in young animals of both genotypes (Fig 1C, left panel), whereas old *Lmna*$^{LCS/LCS}$ mice showed improved glucose tolerance compared to age-matched *Lmna*$^{+/+}$ mice (Fig 1C, right panel). As expected, no differences in basal and glucose-stimulated insulin secretion were observed in young animals from either genotype (Fig 1D, left panel). Basal and stimulated insulin secretion was, however, increased in old *Lmna*$^{LCS/LCS}$ mice compared to old WT mice (Fig 1D, right panel). Altogether, these data suggest that although *Lmna*$^{LCS/LCS}$ mice become obese as they age, their glucose clearance and insulin secretion are improved, suggesting that lamin C may modulate the function of pancreatic islets of Langerhans during aging.

Lmna$^{LCS/LCS}$ mice have increased β-cell mass and insulin secretion during aging

Our observations in aged *Lmna*$^{LCS/LCS}$ mice prompted us to study whether lamin C could contribute to pancreatic islet function by regulating pancreatic mass and/or insulin secretion. Old *Lmna*$^{LCS/LCS}$ mice had heavier pancreata, whereas no differences in mass were observed between genotypes in young animals (Fig 2A). Histological analyses revealed that while young *Lmna*$^{+/+}$ and *Lmna*$^{LCS/LCS}$ pancreata were microscopically similar, pancreata from old *Lmna*$^{LCS/LCS}$ mice displayed significantly larger islets of Langerhans compared to *Lmna*$^{+/+}$ mice (Fig 2B). This effect was further amplified in the pancreata of “very old” (141 weeks old) *Lmna*$^{LCS/LCS}$ mice, as evidenced by hyperplasic islets (Supplemental data 1C). In young animals, measurements of islet size (Fig 2C, upper panel) and staining of insulin and glucagon-positive cells within the pancreatic islets (Fig 2D, upper panel) revealed no differences, whereas old *Lmna*$^{LCS/LCS}$ animals displayed enlarged islets with an increase in insulin-positive cells, but no differences in the number of glucagon-positive cells (Fig 2C and 2D, lower panel). Quantification of the β-/α-cell ratio confirmed an increased number of insulin-positive β-cells in aged *Lmna*$^{LCS/LCS}$ mice (Fig 2E)

whereas no changes were observed on glucagon-positive α-cells (Supplemental data 2A). In addition, when compared to young mice, old *Lmna*$^{LCS/LCS}$ mice exhibited an increased number of islets per pancreas (Fig 2F). Furthermore, total pancreatic insulin level was increased in LCS mice compared to control mice (Fig 2G) whereas global glucagon level was not significantly different (supplemental data 2B). These data demonstrate that the expression of lamin C protects from aging-induced β-cell mass loss by increasing the size and the number of islets of Langerhans and the number of insulin-positive cells.

We then investigated the functionality of these abundant and large *Lmna*$^{LCS/LCS}$ islets through glucose-stimulated insulin secretion (GSIS) experiments. Although no difference in GSIS between genotypes was observed in pancreatic islets isolated from young animals, islets derived from old *Lmna*$^{LCS/LCS}$ mice displayed a 29.5% higher GSIS than age-matched control islets after 20mM glucose stimulation (Fig 2H). Interestingly, no difference of insulin secretion in basal, 2.8mM glucose stimulation was observed, suggesting that the increased insulinemia observed in fasted *Lmna*$^{LCS/LCS}$ mice (Fig 1D) could be due to a cumulative effect of the increased number of islets and their improved insulin secretion capacity.

To confirm the direct effect of lamin C on β-cells, we next generated MIN6 pancreatic β-cell lines in which lamin A expression was abolished using CRISPR/Cas9-mediated genome editing (MIN6^{LCO}). Targeting exon 11 of the *Lmna* gene resulted in a complete depletion of lamin A expression. In the MIN6^{LCO} cells expressing only lamin C (Supplemental data 3A) insulin secretion in response to a 20mM glucose stimulation was increased compared to the control MIN6^{WT} cells (Supplemental data 3B), indicating that lamin C can enhance insulin secretion and improve β-cell function.

Taken together, these results showed that old *Lmna*$^{LCS/LCS}$ mice have increased β-cell number and improved insulin secretion in response to glucose both *in vitro* and *in vivo*. These

adaptive mechanisms may account for the normoglycemia observed in old *Lmna*$^{LCS/LCS}$ mice despite their obesity.

Increased insulin secretion in *Lmna*$^{LCS/LCS}$ mice can counteract obesity-induced type 2 diabetes

To counteract obesity, β-cells need to increase their secretory capacity by progressive expansion of their mass (12). To evaluate how *Lmna*$^{LCS/LCS}$ β-cell function adapts to metabolic challenges, we investigated the capacity of *Lmna*$^{LCS/LCS}$-derived islets to counteract hyperglycemia observed during obesity-induced T2D in young mice. Challenging 12 weeks old *Lmna*$^{+/+}$ and *Lmna*$^{LCS/LCS}$ mice with a 60%kcal high-fat diet (HFD) for 25 weeks resulted in increased body weight (Fig 3A). This body weight gain was significantly higher in *Lmna*$^{LCS/LCS}$ mice and was associated to increased food intake when compared to the control mice (Supplemental data 4). No differences were observed between genotypes in the consumption of regular chow diet (CD). Monitoring of fasting glycemia over the course of HFD revealed that during the first 10 weeks, *Lmna*$^{LCS/LCS}$ mice were hyperglycemic compared to control mice, probably due to their higher body weight (Fig 3B). However, at week 15 under HFD, a significant improvement in fasting glycemia was observed. At week 25, *Lmna*$^{LCS/LCS}$ mice demonstrated a further improvement in glucose tolerance (Fig 3C) and showed increased insulin secretion in response to *in vivo* glucose stimulation (Fig 3D). GSIS experiments using islets isolated from HFD-fed mice for 25 weeks demonstrated that while *Lmna*$^{+/+}$-derived islets failed to secrete insulin in response to glucose, islets from HFD-fed *Lmna*$^{LCS/LCS}$ mice efficiently secreted insulin in response to glucose (Fig 3E).

These results demonstrate that *Lmna*$^{LCS/LCS}$ mice efficiently counteract HFD-induced hyperglycemia by increasing insulin secretion. Taken together with our aging studies, these

results suggest that a lamin C-specific adaptive mechanism is engaged by insulin-producing cells to maintain glucose responsiveness in order to counteract the effects of aging and obesity-induced T2D.

Increased β-cell regeneration in streptozotocin-injected *Lmna*$^{LCS/LCS}$ mice

To further explore the role of lamin C on β-cell number and function, we evaluated the capacity of *Lmna*$^{LCS/LCS}$ mice to regenerate β-cells in an acute β-cell loss context. 13 weeks old *Lmna*$^{+/+}$ and *Lmna*$^{LCS/LCS}$ animals were treated with a single dose of streptozotocin (STZ, 200 mg/kg) to mimic diabetes, and the regeneration of β-cells was measured 18 days after STZ injection. 3 days after STZ treatment, *Lmna*$^{+/+}$ and *Lmna*$^{LCS/LCS}$ mice became diabetic with no significant difference in fasting glucose level (Fig 4A). From day 4, while *Lmna*$^{+/+}$ mice remained hyperglycemic, blood glucose levels in *Lmna*$^{LCS/LCS}$ mice rapidly decreased with a complete normalization of glycemia 18 days after STZ injection. Moreover, we observed approximately 15% of body weight loss during the first 4 days following STZ treatment for both genotypes. 18 days after STZ injection *Lmna*$^{+/+}$ mice remained as leaner as they were before the treatment, while *Lmna*$^{LCS/LCS}$ mice recovered their initial body weight (Supplemental data 5A). Consistent with our previous observations, *Lmna*$^{LCS/LCS}$ showed improved glucose tolerance 18 days after STZ injection (Fig 4B), suggesting functional insulin-producing cells in STZ-treated *Lmna*$^{LCS/LCS}$ mice.

Morphological analysis of the pancreata 18 days post-STZ injection revealed that the number of insulin-positive cells was dramatically reduced in *Lmna*$^{+/+}$ islets (Fig 4C, left panel). Conversely, *Lmna*$^{LCS/LCS}$ insulin-positive β-cells recovered efficiently, with comparable staining of insulin- and glucagon-positive cells before and after STZ treatment. Overall, 18 days after STZ

injection, a 2.5-fold increase in insulin-positive cells was observed in the pancreas of *Lmna*$^{LCS/LCS}$ mice compared to control mice (Fig 4C, right panel).

The increased number of islets in *Lmna*$^{LCS/LCS}$ mice led us to hypothesize that *Lmna*$^{LCS/LCS}$ mice are either protected from STZ-induced apoptosis and/or are able to efficiently regenerate β-cells after STZ-induced damage. 72h after STZ treatment, β-cells were strongly depleted equally in *Lmna*$^{+/+}$ and *Lmna*$^{LCS/LCS}$ mice as shown by representative immunostaining as well as β-cells mass quantification (Fig 4D). The susceptibility of β-cells to STZ-induced apoptosis was confirmed by immunostaining (Supplemental data 5B, left panel), and quantitative assessments 48h after STZ treatment using TUNEL assays showed no significant difference in the number of apoptotic cells between *Lmna*$^{+/+}$ and *Lmna*$^{LCS/LCS}$ mice (Supplemental data 5B, right panel). This finding was further confirmed in the MIN6 β-cell line treated with STZ, in which no differences in the number of apoptotic cells were observed between MIN6^{WT} and MIN6^{LCO} cells (Supplemental data 5C).

We next studied β-cell regeneration after STZ treatment in *Lmna*$^{LCS/LCS}$ mice. The presence of proliferating cells after STZ treatment was quantified using phospho-histone H3 (phosho-H3) antibody staining on pancreatic sections at day 9 post-STZ injection. Pancreata from *Lmna*$^{LCS/LCS}$ mice had a significantly higher number of phospho-H3 positive cells compared to control mice (Fig 4E), suggesting an increased regenerative capacity in *Lmna*$^{LCS/LCS}$ mice. To identify the functional profile of these newly generated cells, we next performed co-immunostaining for phosho-H3 (red) and different pancreatic markers, including insulin (β-cells), lectin (ductal cells), glucagon (α-cells) and somatostatin (δ-cells). Co-immunostaining was observed for phosho-H3 and insulin, as well as lectin but not with glucagon or somatostatin, suggesting that proliferating cells observed in *Lmna*$^{LCS/LCS}$ mice may arise from duplication of

pre-existing β-cells and from ductal cells (Fig 4F) two well-known processes for β-cell neogenesis (8).

Altogether, these results suggest that *Lmna*$^{LCS/LCS}$ mice are able to counteract STZ-induced diabetes by regenerating β-cells.

Lmna$^{LCS/LCS}$ mice display a transcriptional reprogramming of genes involved in mitochondria and translation

Given the important role of lamins in chromatin organization and in the control of gene expression (4), we next evaluated the transcriptional status, DNA methylation and chromatin accessibility of islets isolated from 75 weeks old *Lmna*$^{+/+}$ and *Lmna*$^{LCS/LCS}$ mice. RNA-sequencing based analysis (RNA-seq) revealed that 1507 genes (9.3% of the sequenced genes) were significantly differentially regulated between genotypes (p-value<0.05), with 1024 genes upregulated and 483 genes downregulated in *Lmna*$^{LCS/LCS}$ mice relative to controls (Fig 5A). Gene ontology enrichment analysis showed an enrichment of genes associated with mitochondria (15.92%) and global translation (15.59%). Most genes associated with mitochondrial function (205/240 genes) and translation pathways (169/235 genes) were significantly upregulated in *Lmna*$^{LCS/LCS}$ islets compared to *Lmna*$^{+/+}$ islets. Reduced representation bisulfite sequencing (RRBS)-based methylome analysis revealed that the observed variations in gene expression were not correlated to changes in DNA methylation (Fig 5B). Indeed, independent of the region of the genome that was analyzed (Supplemental data 6), no differentially methylated cytosines (DMC) were found in 1383868 cytosines tested. Moreover, no differentially methylated regions (DMR) were found in 872305 tested regions (GEO accession number: GSE122361). In order to evaluate whether the transcriptional dysregulation was due to a global remodelling of the chromatin compaction and/or accessibility, we performed Assay for Transposable-Accessible

Chromatin with high-throughput sequencing (ATAC-seq) on pancreatic islets isolated from old *Lmna*$^{+/+}$ vs *Lmna*$^{LCS/LCS}$ mice. ATAC-seq results revealed that no difference in chromatin accessibility profiles were observed between *Lmna*$^{+/+}$ and *Lmna*$^{LCS/LCS}$ isolated islets (Fig 5C), suggesting that the transcriptional dysregulations observed in RNA-seq analysis were not due to changes in global chromatin accessibility upon the exclusive expression of lamin C.

To go further into the molecular mechanisms by which lamins could modulate transcription programs, we analyzed the chromatin architecture by investigating the spatial nuclear localization of selected histone marks that are known to modulate gene expression (13). Immunofluorescence analyses of pancreatic sections showed an enrichment of the active enhancer mark H3K27Ac at the nuclear periphery in *Lmna*$^{LCS/LCS}$ β-cells compared to control (Fig 5D, left panel) whereas no difference was observed for the localization of the repressive mark H3K9Me3 (Fig 5D, right panel). Interestingly, the distribution of the H3K27Ac epigenetic mark to the nuclear periphery is associated with a modification of the nuclear architecture. Indeed, we observed that the chromatin is relocated to the periphery of the nucleus in *Lmna*$^{LCS/LCS}$ mice as indicated by Hoechst staining (fig 5D) without changing the global chromatin accessibility as shown by our ATAC-seq analysis.

Taken together, our transcriptomic and epigenomic wide studies demonstrate that the transcriptional reprogramming of genes involved in mitochondrial function and global translation cannot be assigned to either changes in DNA methylation or chromatin accessibility signatures (RRBS and ATAC-seq) but more likely to the relocalisation of epigenomic marks and/or a remodeling of the nuclear architecture.

Lmna$^{LCS/LCS}$ pancreatic islets display increased mitochondrial biogenesis and increased global translation

Since mitochondrial homeostasis is critical for both the maintenance of β-cell function and lifespan promotion (14), we next focused on the regulation of mitochondrial gene expression and function. First, we validated our RNA-seq data by quantitative RT-PCR analysis and confirmed that *Lmna*$^{LCS/LCS}$-derived islets expressed increased levels of key genes involved in the control of mitochondrial function, including the genes encoding electron transport chain proteins (Nduf, Atp5 and Cox protein family, Fig 6A). In addition, the amount of mitochondrial DNA relative to nuclear DNA was significantly higher in *Lmna*$^{LCS/LCS}$ islets (Fig 6B). Ultrastructural analysis of β-cells by transmission electron microscopy (Fig 6C) together with the oxygen consumption rate (OCR) of islets (Fig 6D) further supported a higher number of functional mitochondria in *Lmna*$^{LCS/LCS}$ islets. Taken together, these results suggest that both mitochondrial number and activity are increased in pancreatic islets isolated from *Lmna*$^{LCS/LCS}$ mice.

RNA-seq data also highlighted a role for lamin C in the regulation of protein translation-related genes in islets from old *Lmna*$^{LCS/LCS}$ mice. In particular, genes involved in ribosome synthesis (Rpl and Mrpl protein family) and in the initiation phase of eukaryotic translation (eIFs, eukaryotic initiation factor) were overexpressed in *Lmna*$^{LCS/LCS}$ islets. qPCR experiments confirmed that the expression of genes directly implicated in different steps of translation was significantly increased in *Lmna*$^{LCS/LCS}$ islets compared to *Lmna*$^{+/+}$ islets (Fig 6E). Because ribosome synthesis is tightly correlated with ribosomal RNA (rRNA) synthesis, we also measured 18S and 28S rRNA levels in isolated islets and found that their expression levels were 1.5-fold increased in *Lmna*$^{LCS/LCS}$ islets (Fig 6F). To confirm that translation rates are increased in *Lmna*$^{LCS/LCS}$ islets, we measured ^{35}S-Met/Cys incorporation and found that global protein synthesis levels were significantly increased in *Lmna*$^{LCS/LCS}$ islets (Fig 6G). Since insulin is the major protein synthetized in β-cells, we measured insulin content in *Lmna*$^{+/+}$ and *Lmna*$^{LCS/LCS}$ isolated islets. Since *Lmna*$^{LCS/LCS}$ islets are larger than control islets, classical insulin content

measurement may not quantitatively reflect the abundance of insulin per cell. Therefore, we performed FACS analysis to measure intracellular insulin levels in dissociated β-cells. As shown in Fig 6H, quantification of FACS experiments revealed that insulin production was increased by approximately 25% in *Lmna*$^{LCS/LCS}$ β-cells.

Altogether, these data suggest that the increased insulin secretion observed in *Lmna*$^{LCS/LCS}$ mice is likely due to an increase in global translation rates, which enhances insulin production. The secretion is supported by an increased number of functional mitochondria that play a crucial role in insulin exocytosis upon glucose stimulation.The observed lamin C-mediated increase in insulin production and secretion may explain the improved metabolic phenotype observed in obese, aged *Lmna*$^{LCS/LCS}$ mice.

Discussion

Loss of β-cell function and mass is involved in the development of T1D and T2D, and may contribute to the metabolic complications observed during aging. Our results demonstrate for the first time that the exclusive expression of lamin C acts as a key regulator of β-cell function and regeneration, thus protecting against hyperglycemia observed in several forms of metabolic stresses, such as aging, diet-induced obesity and STZ-induced diabetes. By combining *in vitro*, *ex vivo* and *in vivo* studies, we report that lamin C expression increases β-cell number during aging, counteracts β-cell failure during diet-induced obesity and promotes β-cell regeneration after STZ treatment. Most importantly we demonstrate that lamin C modulates a specific transcriptional program that contributes to enhance the translation of insulin and promotes insulin secretion through a mitochondria-coupled mechanism.

It has been shown that β-cell turnover decreases with aging due to the onset of senescence (15). Indeed, the expression of *p16*^{Ink4a}, a key marker of senescence, limits islet

proliferation and regeneration in an age-dependent manner (16). Conversely, the downregulation of $p16^{Ink4a}$ in a *Pten*-null background reduces the age-induced decline of β-cell proliferation and enhances islet mass in aged mice (17), as observed in our aged $Lmna^{LCS/LCS}$ mice. While one may speculate that a decrease in cellular senescence in our $Lmna^{LCS/LCS}$ mice may underlie the observed maintenance of β-cell mass during aging, no difference in the expression of the senescence marker $p16^{Ink4a}$ was observed in our $Lmna^{LCS/LCS}$ mice versus controls (data not shown), suggesting that delayed senescence does not contribute to the maintenance of functional islets in our model. This hypothesis is further strengthened by the observation that β-cells which exclusively express lamin C adapt to pathological conditions unrelated to aging, such as diabetes induced in young mice.

The specific functions of lamin A versus lamin C in β-cell maintenance and function during aging and/or metabolic stress is a central question. A limitation of the $Lmna^{LCS/LCS}$ model is that we cannot rule out potential contributing effects of lamin C in other organs, as well as an effect of lamin A deficiency in cells expressing lamin C only. Since the gene targeting strategy employed here to generate the $Lmna^{LCS/LCS}$ model precludes to specifically express lamin C only in β cells, and subsequently perform lineage-tracing experiments, this question remains to be addressed. Interestingly, mice expressing lamin A only ($Lmna^{LAO}$) are healthy with no detectable phenotypical or histopathological abnormalities, despite a complete loss of lamin C expression (18), even in 24-month-old mice. Challenging these $Lmna^{LAO}$ mice with HFD or STZ treatment may help to accurately characterize their specific functions in glucose homeostasis.

To decipher the molecular mechanism by which lamin C regulates pancreatic islet functions, we analyzed the impact of lamin C exclusive expression using genome-wide DNA methylation, ATAC-seq and high-throughput RNA sequencing.

RNA-seq analysis revealed that the expression of genes involved in mitochondrial function and protein translation was altered in aged *Lmna*$^{LCS/LCS}$ islets compared to controls. Unlike the decline of mitochondrial function observed in aging-associated diseases such as diabetes (14), we found increased mitochondrial activity in aged *Lmna*$^{LCS/LCS}$ islets that likely contributes to the observed improvement in insulin secretion. It is interesting to note that decreased mitochondrial biogenesis was previously observed in adipose tissue from *Lmna*$^{LCS/LCS}$ mice aged 45 weeks (6). Contrary to white adipose tissue where mitochondria are relatively less abundant and crucial for adipocyte homeostasis in normal diet and temperature conditions, mitochondrial function in the β-cell is directly coupled to insulin biosynthesis and insulin exocytosis. Since both studies were not conducted in animals at the same ages (45 weeks (6) vs 75 weeks old in the present study), we cannot exclude an age-dependent effect in these tissues. We can however propose that the differential expression of lamin isoforms may have a tissue-specific impact on mitochondrial gene transcription.

RNA-seq analysis and translation rate analysis revealed an increase of global protein synthesis in the islets of aged-*Lmna*$^{LCS/LCS}$ associated with an increased lifespan as described in our previous study (6). It is widely accepted that reduced protein synthesis promotes longevity (19). Indeed, protein biosynthesis in aging is accompanied by more frequent production of damaged proteins due to transcriptional or translational errors and co-translational protein misfolding. The increased lifespan associated to an upregulation of global protein synthesis in our aged-*Lmna*$^{LCS/LCS}$ mice suggests that proteins synthetized within the pancreatic islets are well-folded and biologically active, possibly due to the maintenance of an efficient protein quality control system. This hypothesis is supported by our demonstration that insulin, the major protein synthesized by β-cells, is properly secreted and efficient during aging, since aged-*Lmna*$^{LCS/LCS}$ mice remain glucose tolerant and normoglycemic. This functional insulin

overproduction may contribute to the maintenance of a positive feedback loop of insulin-regulated protein synthesis *via* the mTOR pathway (20).

How *Lmna* isoforms are able to modulate gene transcription in β-cells remains to be elucidated. Previous studies have described epigenetic dysregulation in pancreatic islets during T2D, showing differential methylation pattern associated with islet dysfunctions (21) and changes in the open chromatin landscape of human islets (22). Moreover, DNA methylation is a dynamic process in aging β-cells. *De novo* methylation of proliferation-related genes and demethylation of genes related to β-cell function increases insulin secretion during aging (23). Nevertheless, we did not observe any difference in DNA methylation in $Lmna^{LCS/LCS}$ versus wild type pancreatic islets. This finding shows that the selective expression of lamin C does not influence overall DNA methylation in pancreatic islets and points to another regulatory mechanism.

In metazoan nuclei, specific lamina-associated domains (LADs) contribute to the overall spatial organization of the genome and are associated with gene repression (24). Cellular defects in cells from progeria patients include widespread alterations in chromatin organization, such as the loss of heterochromatin domains and changes in epigenetic markers (25). Furthermore, it has been shown that lamin A/C can modulate transcription through the regulation of epigenetic factors (26). Therefore, the expression of only one *Lmna* isoform may have a crucial impact on the spatial compartmentalization of inactive or active chromosome domains, which in turn may have consequences on transcriptional dysregulation. Surprisingly, we did not observe any global changes in chromatin accessibility through ATAC-seq experiments in our mouse models. Nevertheless, $Lmna^{LCS/LCS}$ pancreas show an active enhancer mark (H3K27Ac) relocalization to peripheral heterochromatin. The localization of an active histone mark in an heterochromatin environment has already been described showing that

acetylation of histone in silent domains drive their mislocalization and derepression (27). Furthermore, there is increasing evidence for active and regulated transcription in the heterochromatin at the nuclear periphery (28). Altogether, these observations lead us to speculate that the phenotype observed in *Lmna*$^{LCS/LCS}$ mice could be due to transcriptional reactivation of a subset of mitochondrial and translational genes through histone marks relocalization rather than by reorganizing global chromatin accessibility or modifying DNA methylation. The role of lamin C in the nuclear localization of specific loci and their respective histone marks requires further investigations.

In conclusion, *Lmna*$^{LCS/LCS}$ mice present an enhanced adaptive response to the increased metabolic demands during the course of diabetes and aging. This is probably due to efficient glucose-sensing and insulin production by their neogenerated islets (29). Our study reveals an important role for lamin C in pancreatic β-cells, namely a protective role against metabolic defects arising from β-cell dysfunction. This effect may promote the healthy aging of the *Lmna*$^{LCS/LCS}$ mice, and sustain their extended lifespan (6). The discovery of new drugs targeting *Lmna* alternative splicing may represent an innovative therapeutic strategy to counteract aging β-cell decline and improve diabetes treatment.

Acknowledgements

This work was supported by grants from OSEO-ISI CaReNA (I 13 03 008W to JT), from E.G.I.D (ANR-10-LABX-46 to J-S. A.), ANR (BETAPLASTICITY, ANR-17-CE14-0034 to J-S. A.), EFSD (J-S.A.), I-SITE ULNE (EpiRNA-Diab to J-S. A.), Société Francophone du Diabetes (J-S.A.), INSERM, CNRS, Lille University, Association pour la Recherche sur le Diabète (to J-S.A.), Conseil Régional Hauts de France and Métropole Européenne de Lille (to X.G. and J-S.A.) and from the Swiss National Science Foundation (Ambizione PZ00P3-168077 to ICLM). We thank David Lleres and Cyril Esnault for discussions and scientific critique. The authors are grateful to MRI and RHEM for assistance in cytometry and experimental histology, as well as the animal facility platforms RAM and ZEFI. We especially thank Sylvain de Rossi, Myriam Boyer and Chantal Cazevieille for their technical assistance. We thank Magali A. Ravier for advice for the islet isolation from mice and Amal Makrini for the bioinformamatics support. Marion de Toledo and Carine Chavey are the guarantors of this work.

Authors' contribution:

CC and MdT designed, performed and interpreted the majority of the experiments. PC performed histological analysis. MP and CB contributed to the RNA-seq and RRBS analysis as well as the bioinformatics analysis. XG gave advice for islet isolation from mice. ICLM contributed to the aging experiments. CC and MdT wrote the manuscript. ICLM, JT and J-SA reviewed and approved the manuscript.

Conflict of interest:

The authors have declared that no conflict of interest exists.

Abbreviations:

AUC: area under the curve, IPGTT: intra peritoneal glucose tolerance test, GSIS: glucose-stimulated insulin secretion, STZ: streptozotocin, T1D: type-1 diabetes, T2D: type-2 diabetes, DIO: diet-induced obesity, HFD: high-fat diet, CD: chow diet, RRBS: Reduced representation bisulfite sequencing.

References

1. Turgay Y, Eibauer M, Goldman AE, Shimi T, Khayat M, Ben-Harush K, et al. The molecular architecture of lamins in somatic cells. Nature [Internet]. 2017;543(7644):261–4. Available from: http://www.ncbi.nlm.nih.gov/pubmed/28241138
2. Bronshtein I, Kepten E, Kanter I, Berezin S, Lindner M, Redwood AB, et al. Loss of lamin A function increases chromatin dynamics in the nuclear interior. Nat Commun [Internet]. 2015;6:1–9. Available from: http://dx.doi.org/10.1038/ncomms9044
3. Melcer S, Hezroni H, Rand E. Histone modifications and lamin A regulate chromatin protein dynamics in early embryonic stem cell differentiation. Nature [Internet]. 2012;3(May):910. Available from: http://www.nature.com/ncomms/journal/v3/n6/abs/ncomms1915.html%5Cnhttp://www.pubmedcentral.nih.gov/articlerender.fcgi?artid=3564597&tool=pmcentrez&rendertype=abstract
4. Soutoglou E, Misteli T. Mobility and immobility of chromatin in transcription and genome stability. Curr Opin Genet Dev [Internet]. 2007 Oct;17(5):435–42. Available from: http://linkinghub.elsevier.com/retrieve/pii/S0959437X07001554
5. Charar C, Gruenbaum Y. Lamins and metabolism. Clin Sci [Internet]. 2016;131(2):105–11. Available from: http://clinsci.org/cgi/doi/10.1042/CS20160488
6. Lopez-Mejia IC, de Toledo M, Chavey C, Lapasset L, Cavelier P, Lopez-Herrera C, et al. Antagonistic functions of LMNA isoforms in energy expenditure and lifespan. EMBO Rep [Internet]. 2014 May;15(5):529–39. Available from: http://www.ncbi.nlm.nih.gov/pubmed/24639560
7. Zhou Q, Melton DA. Pancreas regeneration. Nature [Internet]. 2018 May 16;557(7705):351–8. Available from: http://www.nature.com/articles/s41586-018-0088-0
8. Aguayo-Mazzucato C, Bonner-Weir S. Pancreatic β Cell Regeneration as a Possible Therapy for Diabetes. Cell Metab [Internet]. 2017;1–11. Available from: http://dx.doi.org/10.1016/j.cmet.2017.08.007
9. Elenbaas JS, Bragazzi Cunha J, Azuero-Dajud R, Nelson B, Oral EA, Williams JA, et al. Lamin A/C Maintains Exocrine Pancreas Homeostasis by Regulating Stability of RB and Activity of E2F. Gastroenterology [Internet]. 2018;154(6):1625-1629.e8. Available from: https://doi.org/10.1053/j.gastro.2018.01.024
10. Osorio FG, Navarro CL, Cadiñanos J, López-Mejía IC, Quirós PM, Bartoli C, et al. Splicing-directed therapy in a new mouse model of human accelerated aging. Sci Transl Med [Internet]. 2011 Oct 26 [cited 2014 Jan 30];3(106):106ra107. Available from: http://www.ncbi.nlm.nih.gov/pubmed/22030750
11. Jung H-J, Coffinier C, Choe Y, Beigneux AP, Davies BSJ, Yang SH, et al. Regulation of prelamin A but not lamin C by miR-9, a brain-specific microRNA. Proc Natl Acad Sci [Internet]. 2012;109(7):E423–31. Available from: http://www.pnas.org/cgi/doi/10.1073/pnas.1111780109
12. Weir GC, Bonner-Weir S. Five stages of evolving beta-cell dysfunction during progression to diabetes. Diabetes [Internet]. 2004 Dec;53 Suppl 3(December):S16-21. Available from: http://www.ncbi.nlm.nih.gov/pubmed/15561905
13. Gates LA, Foulds CE, O'Malley BW. Histone Marks in the 'Driver's Seat': Functional Roles in Steering the Transcription Cycle. Trends Biochem Sci. 2017;42(12):977–89.

14. Sebastián D, Palacín M, Zorzano A. Mitochondrial Dynamics: Coupling Mitochondrial Fitness with Healthy Aging. Trends Mol Med [Internet]. 2017;23(3):201–15. Available from: http://dx.doi.org/10.1016/j.molmed.2017.01.003
15. Aguayo-Mazzucato C, van Haaren M, Mruk M, Lee TB, Crawford C, Hollister-Lock J, et al. β Cell Aging Markers Have Heterogeneous Distribution and Are Induced by Insulin Resistance. Cell Metab [Internet]. 2017;25(4):898-910.e5. Available from: http://dx.doi.org/10.1016/j.cmet.2017.03.015
16. Krishnamurthy J, Ramsey MR, Ligon KL, Torrice C, Koh A, Bonner-Weir S, et al. p16INK4a induces an age-dependent decline in islet regenerative potential. Nature [Internet]. 2006;443(7110):453–7. Available from: http://www.ncbi.nlm.nih.gov/pubmed/16957737%5Cnhttp://www.nature.com/nature/journal/v443/n7110/pdf/nature05092.pdf
17. Zeng N, Yang K-T, Bayan J-A, He L, Aggarwal R, Stiles JW, et al. PTEN controls β-cell regeneration in aged mice by regulating cell cycle inhibitor p16ink4a. Aging Cell [Internet]. 2013 Dec [cited 2014 Jan 22];12(6):1000–11. Available from: http://www.ncbi.nlm.nih.gov/pubmed/23826727
18. Coffinier C, Jung H-J, Li Z, Nobumori C, Yun UJ, Farber EA, et al. Direct Synthesis of Lamin A, Bypassing Prelamin A Processing, Causes Misshapen Nuclei in Fibroblasts but No Detectable Pathology in Mice. J Biol Chem [Internet]. 2010 Jul 2;285(27):20818–26. Available from: http://www.jbc.org/lookup/doi/10.1074/jbc.M110.128835
19. Gonskikh Y, Polacek N. Alterations of the translation apparatus during aging and stress response. Mech Ageing Dev [Internet]. 2017;168(March):30–6. Available from: https://doi.org/10.1016/j.mad.2017.04.003
20. Proud CG. Regulation of protein synthesis by insulin. Biochem Soc Trans [Internet]. 2006;34(Pt 2):213–6. Available from: http://www.ncbi.nlm.nih.gov/pubmed/16545079
21. Volkov P, Bacos K, Ofori JK, Lou J, Esguerra S, Eliasson L, et al. Whole-genome Bisulfite Sequencing of Human Pancreatic Islets Reveals Novel Differentially Methylated Regions in Type 2 Diabetes Pathogenesis. 2017;1–47. Available from: http://diabetes.diabetesjournals.org/content/diabetes/early/2017/01/04/db16-0996.full.pdf
22. Bysani M, Agren R, Davegårdh C, Volkov P, Rönn T, Unneberg P, et al. ATAC-seq reveals alterations in open chromatin in pancreatic islets from subjects with type 2 diabetes. Sci Rep. 2019;9(1):1–12.
23. Avrahami D, Li C, Zhang J, Schug J, Avrahami R, Rao S, et al. Aging-Dependent Demethylation of Regulatory Elements Correlates with Chromatin State and Improved β Cell Function. Cell Metab [Internet]. 2015 Oct 6;22(4):619–32. Available from: http://www.ncbi.nlm.nih.gov/pubmed/26321660
24. van Steensel B, Belmont AS. Lamina-Associated Domains: Links with Chromosome Architecture, Heterochromatin, and Gene Repression. Cell [Internet]. 2017;169(5):780–91. Available from: http://dx.doi.org/10.1016/j.cell.2017.04.022
25. McCord RP, Nazario-Toole A, Zhang H, Chines PS, Zhan Y, Erdos MR, et al. Correlated alterations in genome organization, histone methylation, and DNA-lamin A/C interactions in Hutchinson-Gilford progeria syndrome. Genome Res [Internet]. 2013 Feb;23(2):260–9. Available from: http://www.ncbi.nlm.nih.gov/pubmed/23152449
26. Cesarini E, Mozzetta C, Marullo F, Gregoretti F, Gargiulo A, Columbaro M, et al. Lamin A/C sustains PcG protein architecture, maintaining transcriptional repression at target

genes. J Cell Biol. 2015;211(3):533–51.
27. Cabianca DS, Muñoz-Jiménez C, Kalck V, Gaidatzis D, Padeken J, Seeber A, et al. Active chromatin marks drive spatial sequestration of heterochromatin in C. elegans nuclei. Nature [Internet]. 2019;569(7758):734–9. Available from: http://dx.doi.org/10.1038/s41586-019-1243-y
28. Saksouk N, Simboeck E, Déjardin J. Constitutive heterochromatin formation and transcription in mammals. Epigenetics and Chromatin. 2015;8(1):1–17.
29. Wortham M, Sander M. Mechanisms of β-cell functional adaptation to changes in workload. Diabetes, Obes Metab [Internet]. 2016 Sep;18(Suppl 1):78–86. Available from: http://doi.wiley.com/10.1111/dom.12729

Legends

Figure 1: *Lmna*$^{LCS/LCS}$ mice become obese but remain glucose tolerant as they age.

A) Body weight gain curve in *Lmna*$^{+/+}$ and *Lmna*$^{LCS/LCS}$ mice (n=10 per group).

B) Fasting blood glucose in young (25 weeks old) and old (75 weeks old) *Lmna*$^{+/+}$ and *Lmna*$^{LCS/LCS}$ mice (n=5 per group).

C) Intraperitoneal glucose tolerance test (IPGTT) in young and old *Lmna*$^{+/+}$ and *Lmna*$^{LCS/LCS}$ mice (n=5 per group). The bar graphs (inset) represent the area under the curve (AUC).

D) Fasting insulin levels before and after 30 minutes after intraperitoneal glucose injection in young and old *Lmna*$^{+/+}$ and *Lmna*$^{LCS/LCS}$ mice (n=5 per group).

All values are expressed as the mean ± SEM. *p< 0.05, **p< 0.01, ***p< 0.001, n.s not significant by Student's unpaired t-test.

Figure 2: *Lmna*$^{LCS/LCS}$ mice show increased β-cell mass and insulin secretion during aging

A) Pancreas weight in young (25 weeks old, n=6 per group) and old (75 weeks old, n=17 per group) *Lmna*$^{+/+}$ and *Lmna*$^{LCS/LCS}$ mice.

B) Representative images of hematoxylin and eosin (HE) staining of pancreatic sections from young and old *Lmna*$^{+/+}$ and *Lmna*$^{LCS/LCS}$ mice (scale bar, 2 mm). The right image shows a magnification (4X) of the left image.

C) Scatter plot of the diameters of islets of Langerhans from pancreatic sections of young and old *Lmna* $^{+/+}$ and *Lmna*$^{LCS/LCS}$ mice (n=5 animals per group).

D) Representative images from immunofluorescence analysis of pancreatic sections showing co-expression of insulin (green) and glucagon (red) in islets from young and old *Lmna*$^{+/+}$ and *Lmna*$^{LCS/LCS}$ mice (scale bar 100 μm).

E) Quantification of β/α cells ratio per pancreatic section in young and old *Lmna*$^{+/+}$ and *Lmna*$^{LCS/LCS}$ mice (n=4)

F) Quantification of isolated islets number after collagenase digestion in young and old *Lmna*$^{+/+}$ and *Lmna*$^{LCS/LCS}$ mice.

G) Global insulin content from total pancreata of old *Lmna*$^{+/+}$ and *Lmna*$^{LCS/LCS}$ mice (n=6 per group)

H) Glucose-stimulated insulin secretion (GSIS) under low (3mM) or high (20mM) glucose concentration from isolated islets from young and old *Lmna*$^{+/+}$ and *Lmna*$^{LCS/LCS}$ mice (n=4 per group). The results were normalized to total insulin content.

All values are expressed as the mean ± SEM. **p< 0.01, ***p< 0.001, n.s not significant by Student's unpaired t-test.

Figure 3: Increased insulin secretion in *Lmna*$^{LCS/LCS}$ mice can counteract obesity-induced type 2 diabetes

A) Mean body weight from age-matched *Lmna*$^{+/+}$ and *Lmna*$^{LCS/LCS}$ mice (40 weeks old, n=8 per group) fed chow diet (CD) or a high fat diet (HFD) for 25 weeks.

B) Fasting blood glucose levels over time in *Lmna*$^{+/+}$ and *Lmna*$^{LCS/LCS}$ mice (from 15 to 40 weeks old) during HFD (n=8 per group).

C) Intraperitoneal glucose tolerance test (IPGTT) results in *Lmna*$^{+/+}$ and *Lmna*$^{LCS/LCS}$ mice (40 weeks old) fed a HFD for 25 weeks (n=8 per group). The bar graph (inset) represents the area under the curve (AUC).

D) Mean insulin levels before and 30 min after glucose injection in *Lmna*$^{+/+}$ and *Lmna*$^{LCS/LCS}$ mice (40 weeks old) fed a HFD for 25 weeks (n=8 per group).

E) Mean GSIS under low (3mM) or high (20mM) glucose concentration in isolated islets from *Lmna*$^{+/+}$ and *Lmna*$^{LCS/LCS}$ mice (40 weeks old) fed a HFD for 25 weeks (n=8 per group). Insulin secretion is normalized to total insulin content.

All values are expressed as the mean ± SEM. *p< 0.05, **p< 0.01, ***p< 0.001, ****p< 0.0001, n.s not significant by Student's unpaired t-test.

Figure 4: Streptozotocin-injected *Lmna*$^{LCS/LCS}$ mice display increased β-cell regeneration

A) Fasting blood glucose levels after streptozotocin (STZ, at day 0) injection in 13-week-old *Lmna*$^{+/+}$ and *Lmna*$^{LCS/LCS}$ mice (n=5 per group).

B) Blood glucose levels during IPGTT after 16 days of STZ treatment in *Lmna*$^{+/+}$ and *Lmna*$^{LCS/LCS}$ mice (15 weeks old, n=5 per group). The bar graph (inset) represents the area under a curve (AUC).

C) Representative immunostaining images of pancreatic sections from *Lmna*$^{+/+}$ and *Lmna*$^{LCS/LCS}$ mice before and 18 days after STZ injection (n=5 per group) showing co-expression of insulin (green) and glucagon (red). Nuclei are counterstained with Hoechst (left panel) (scale bar 100 μm). Quantification of the mean number of β-cell positive islets/pancreatic section is summarized in the bar graph in (right panel).

D) Representative immunostaining images of pancreatic sections from *Lmna*$^{+/+}$ and *Lmna*$^{LCS/LCS}$ mice 72 hours after STZ injection (n=5 per group) (left panel) showing the destruction of insulin positive b-cells (green) but not glucagon positive a-cells (red). Nuclei are counterstained with Hoechst showing a nuclei free area (white dotted line)(scale bar 100 μm). Quantification of the β-cells /α-cells ratio before and 72h post-STZ injection is represented in right panel.

E) Representative immunostaining images of pancreatic sections from *Lmna*$^{+/+}$ and *Lmna*$^{LCS/LCS}$ mice 9 days after STZ treatment (n=7) showing expression of phospho-histone H3 (red) and insulin (green). Histogramm represents the quantification of the number of phospho-histone H3-positive cells/pancreas section.

F) Representative images of immunostaining of pancreatic sections showing co-expression of specific markers of phospho-histone H3 (red) with either insulin, lectin, glucagon, or somatostatin (top to bottom, green) in *Lmna*$^{LCS/LCS}$ mice. Nuclei are stained with Hoechst (scale bar 100 µm).

All values are expressed as the mean ± SEM. *p< 0.05, **p< 0.01, ***p< 0.001, ****p< 0.0001; ns not significant by Student's unpaired t-test.

Figure 5: *Lmna*$^{LCS/LCS}$ mice display a transcriptional reprogramming of genes involved in mitochondria and translation

A) Heatmap showing genes associated with mitochondrial function (upper panel) and translation (lower panel) with differential expression in isolated islets from old *Lmna*$^{LCS/LCS}$ versus *Lmna*$^{+/+}$ mice (n=9, 3 replicates of 3 mice). The pie chart summarizes the proportion of these classes of genes in the total RNA-seq dataset. The table summarizes the functions of the genes with differential expression in *Lmna*$^{LCS/LCS}$ islets as identified by gene ontology (GO).

B) Scatterplot showing the DNA methylation profile analysed by RRBS of Lmna$^{+/+}$ vs *Lmna*$^{LCS/LCS}$ islets (n=2 per condition).

C) Volcano plot of ATAC-seq from *Lmna*$^{+/+}$ vs *Lmna*$^{LCS/LCS}$ islets. Peaks which P-adj < 0.01 and Log2FC <-1 or >1 are colored in red. Most of the no differential peaks are colored in grey (n=2 per condition).

D) Representative confocal images from immunohistochemistry analysis of pancreatic sections showing co-expression of insulin (red), H3K27Ac, H3K9Me3 (green) and Hoechst staining (grey) in islets from old *Lmna*$^{+/+}$ vs *Lmna*$^{LCS/LCS}$ mice (scale bar 20 µm). The enlarged cells presented in the insert are indicated by a white arrow.

Figure 6: *Lmna*$^{LCS/LCS}$ pancreatic islets display increased mitochondrial biogenesis and increased global translation

A) Relative expression levels of mitochondrial genes assessed by RT-qPCR in isolated islets from old *Lmna*$^{+/+}$ and *Lmna*$^{LCS/LCS}$ mice (n=8 per group).

B) Quantification of mitochondrial DNA levels by qPCR of *mt16s* and *mtND5* gene normalized to genomic DNA in isolated islets from old *Lmna*$^{+/+}$ and *Lmna*$^{LCS/LCS}$ mice (n=8 per group).

C) Representative transmission electron microscopy images at x22000 magnification showing a higher number of mitochondria in *Lmna*$^{LCS/LCS}$ β-cells relative to control cells (n=3 per group).

D) Mean oxygen consumption rate (OCR) are presented in basal conditions and following sequential injection of glucose, oligomycin, FCCP and rotenone determined with a Seahorse XFe96 flux analyzer in isolated islets from old *Lmna*$^{+/+}$ and *Lmna*$^{LCS/LCS}$ mice (n=4 per group).

E) Relative expression levels of translation-related genes assessed by RT-qPCR in isolated islets from old *Lmna*$^{+/+}$ versus *Lmna*$^{LCS/LCS}$ mice (n=8 per group).

F) Relative 18S and 28S rRNA expression assessed by RT-qPCR in isolated islets from *Lmna*$^{+/+}$ and *Lmna*$^{LCS/LCS}$ mice (n=8 per group).

G) Analysis of global translation rates assessed by ^{35}S-Met/Cys incorporation in isolated islets from *Lmna*$^{+/+}$ and *Lmna*$^{LCS/LCS}$ mice (n=7 per group). The scatter plot depicts the mean fold change in protein synthesis.

H) Insulin content evaluated by FACS analysis of dissociated islets from old *Lmna*$^{+/+}$ and *Lmna*$^{LCS/LCS}$ mice (insulin/Alexa 647 staining) (n=4 per group)(left panel). The mean insulin of dissociated islets from old *Lmna*$^{+/+}$ and *Lmna*$^{LCS/LCS}$ mice was quantified (right panel).

All values are expressed as the mean ± SEM. *p< 0.05, **p< 0.01, ***p< 0.001, ****p< 0.0001 by Student's unpaired t-test.

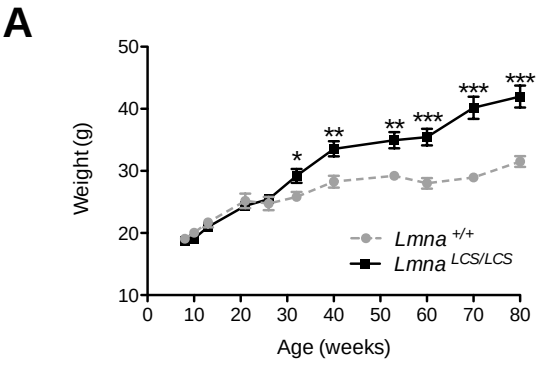

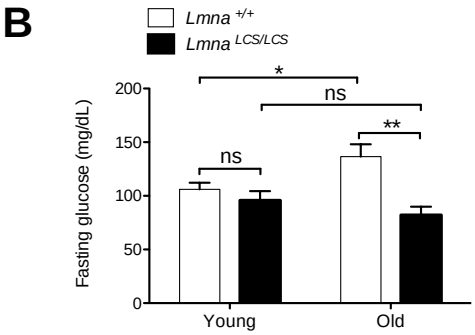

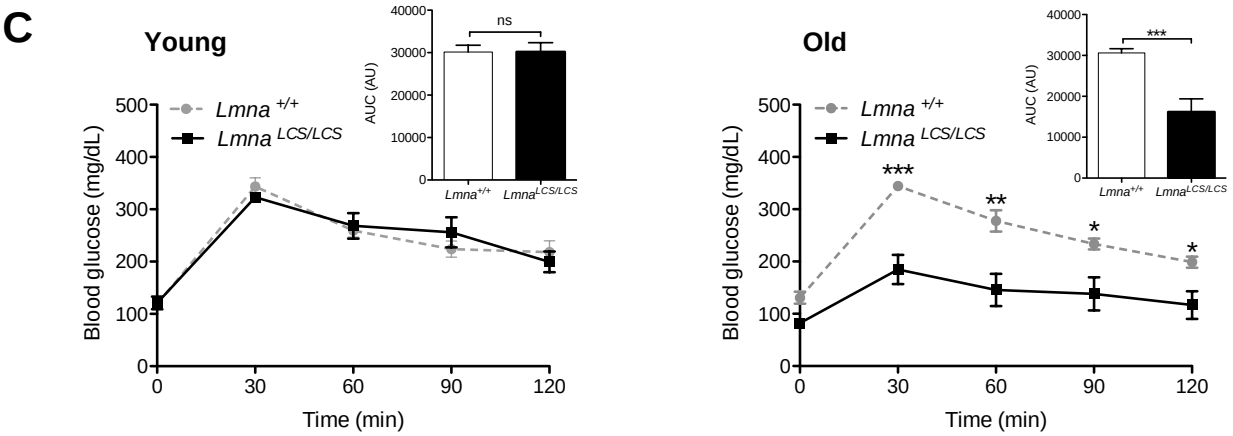

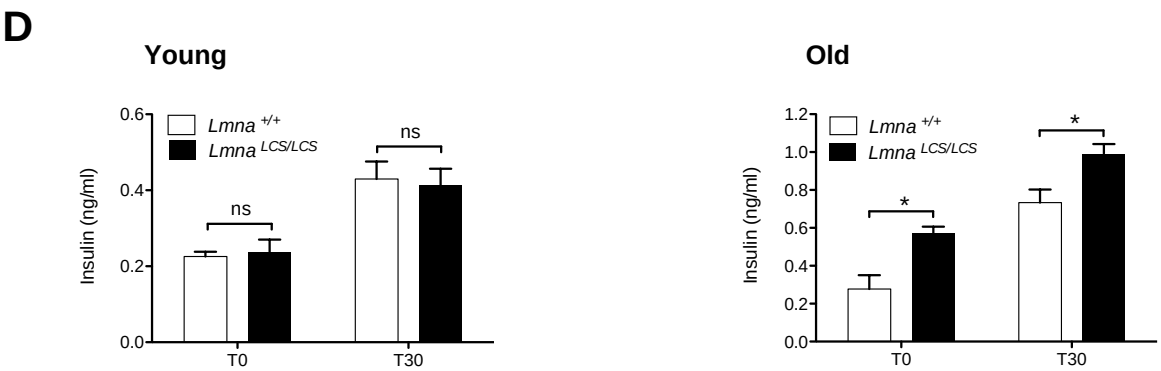

de Toledo et al. Fig 1

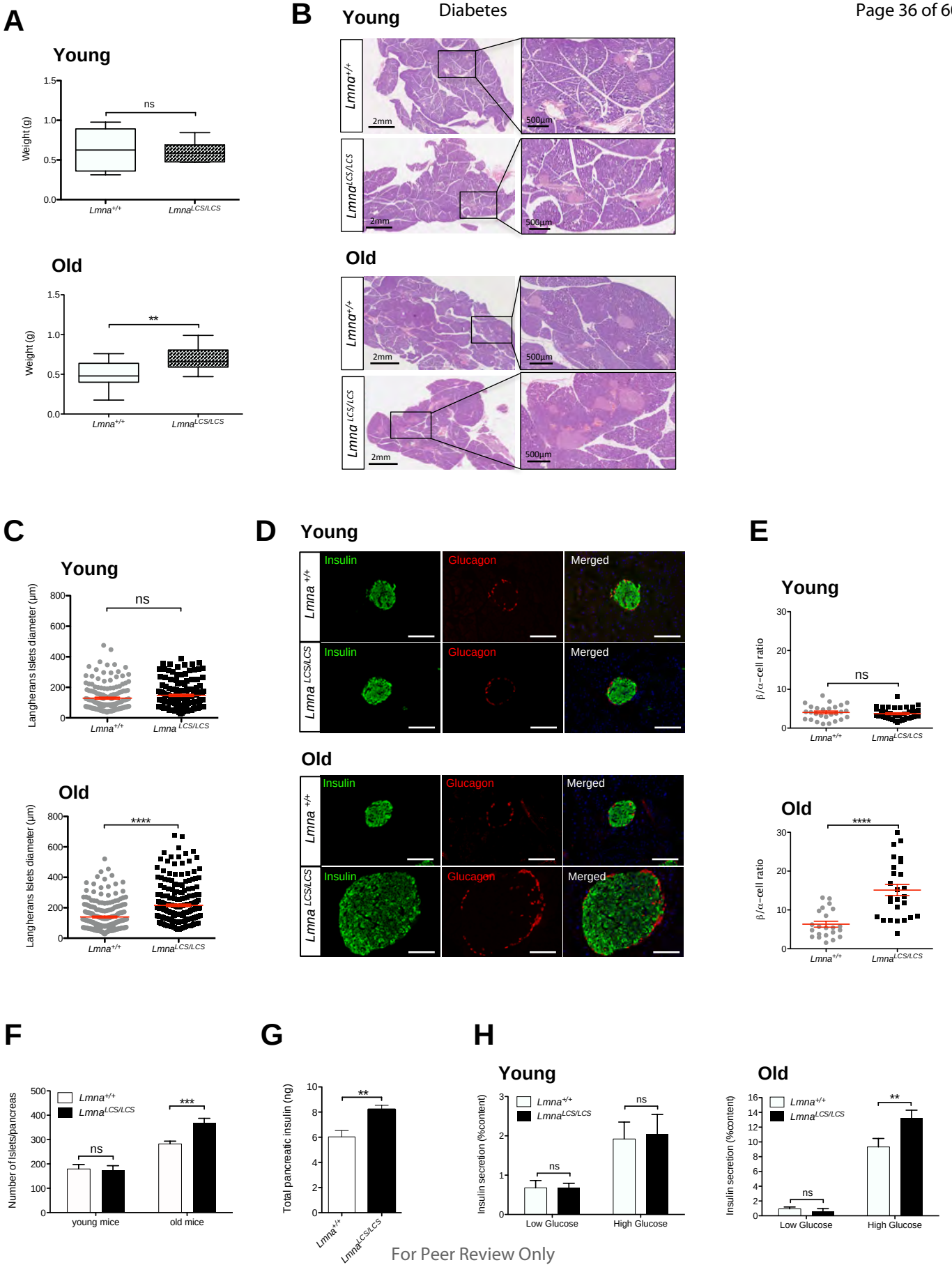

For Peer Review Only

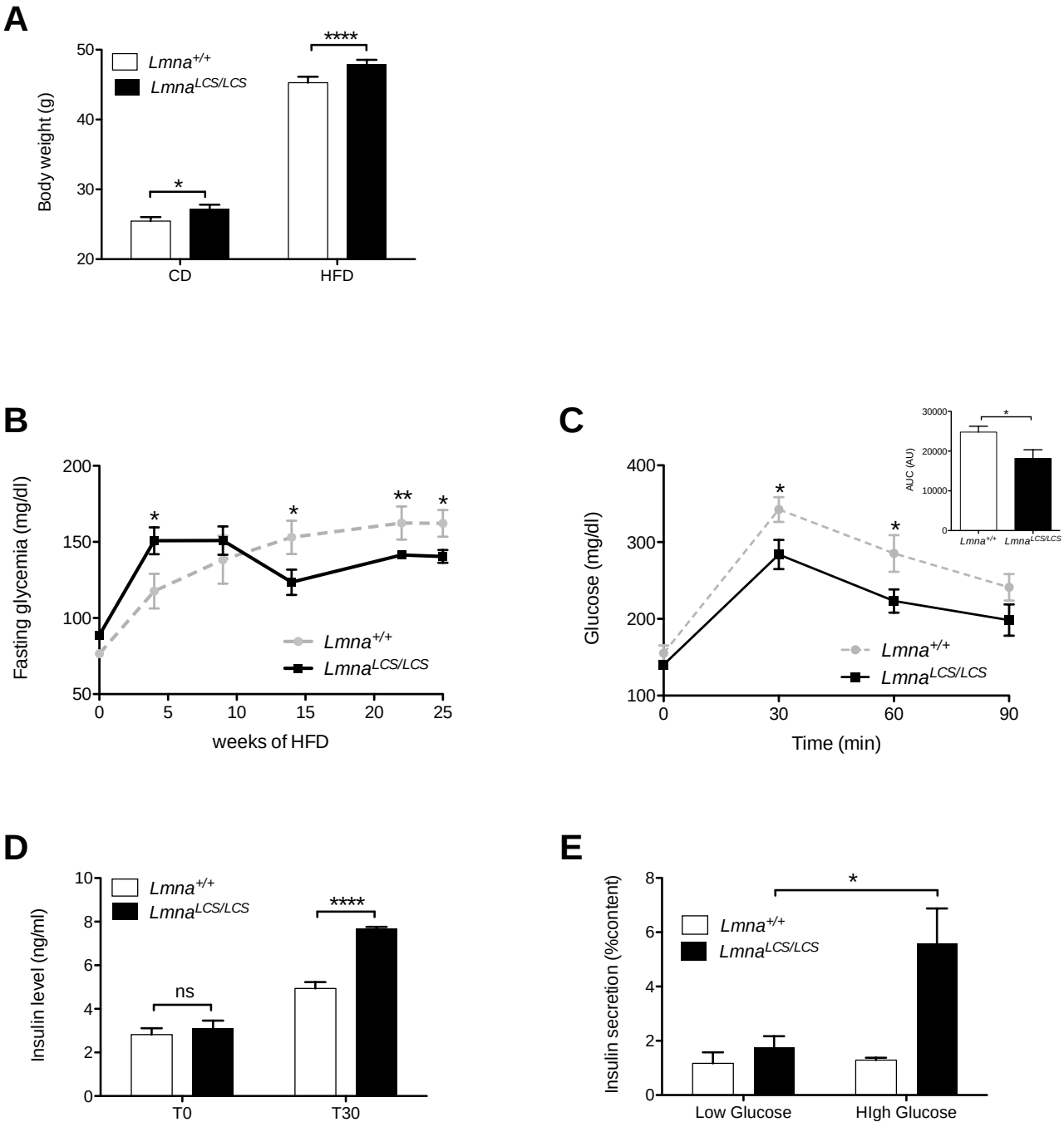

de Toledo et al. Fig 3

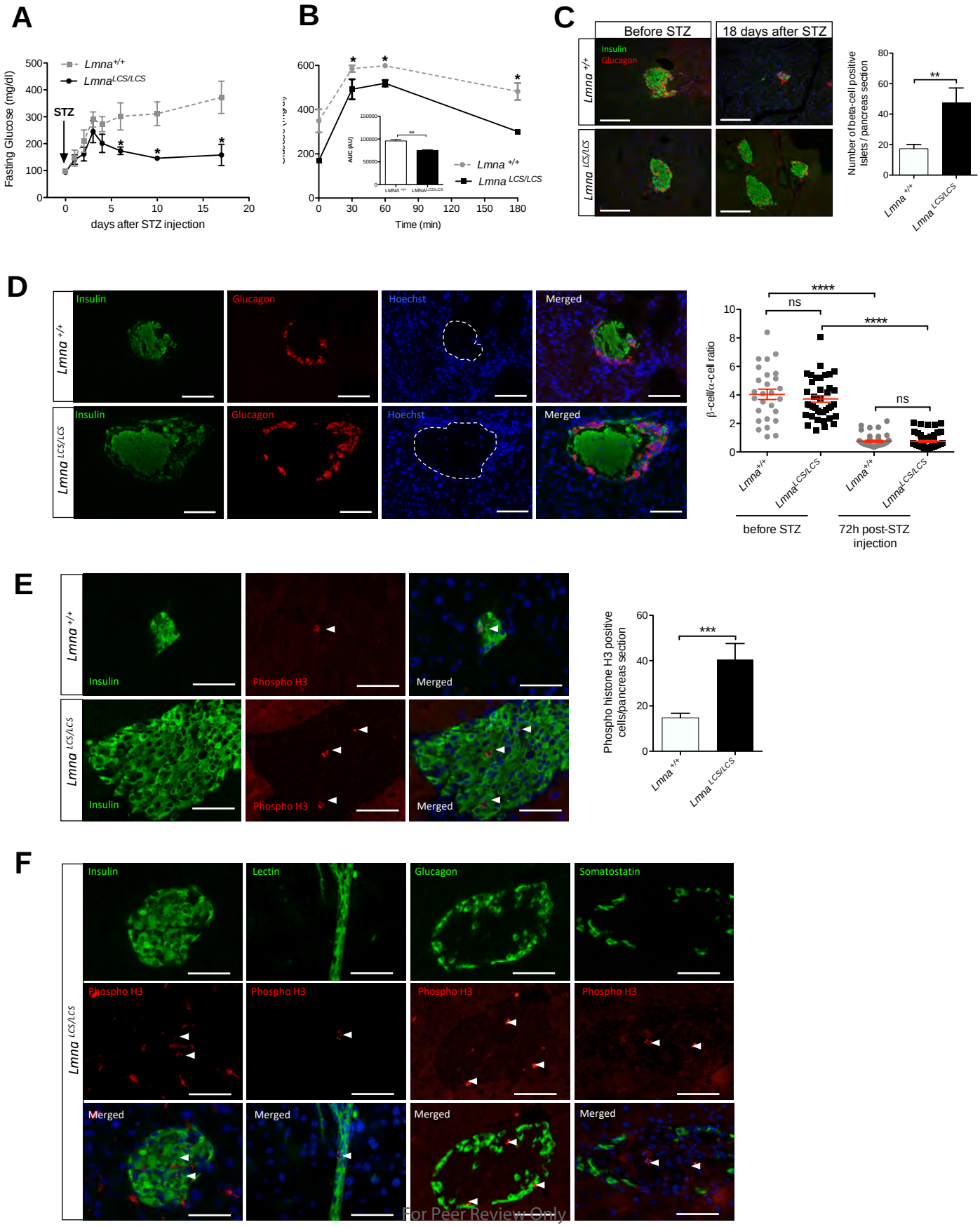

For Peer Review Only

de Toledo et al. Fig 4

A

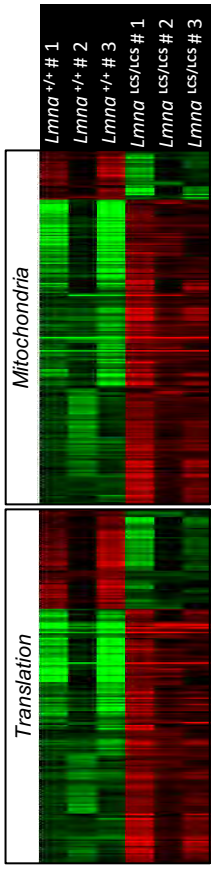

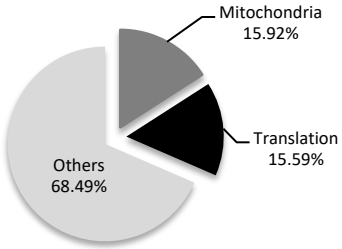

GO Term	Dysregulated genes in GO term	Annotated genes in GO term	p-value
Translation	57	648	1,9E-20
oxidation-reduction process	41	898	9,8E-05
rRNA processing	14	170	5,2E-03
Ribosome assembly	13	58	1,8E-11
Nucleosome assembly	13	104	3,4E-08
Mitochondrial ATP synthesis coupled electron transport	10	40	1,4E-08
mitochondrial transmembrane transport	8	41	5,2E-06
mitochondrial respiratory chain complex assembly	8	39	3,1E-07
Mitophagy in response to mitochondrial depolarisation	7	131	78,2E-03
maturation of SSU-rRNA from tricistronic rRNA transcript (SSU-rRNA, 5.8S rRNA, LSU-rRNA)	6	35	2,9E-05
positive regulation of release of cytochrome c from mitochondria	5	26	7,7E-05
inner mitochondrial membrane organization	4	21	4,3E-04
ATP synthesis coupled proton transport	4	22	5,2E-04
regulation of appetite	4	23	6,2E-04
Positive regulation of insulin secretion involved in cellular response to glucose stimulus	4	32	2,2E-03
outer mitochondrial membrane organization	3	9	7,9E-03
protein maturation by protein folding	2	5	2,9E-03
Nucleosome positioning	2	8	7,9E-03

B

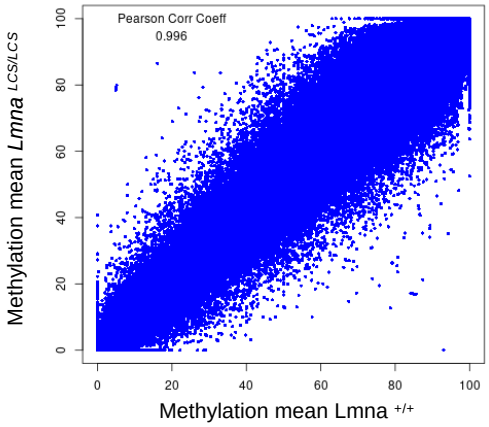

C

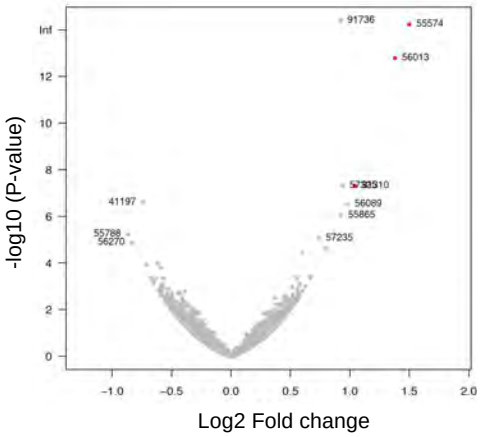

D

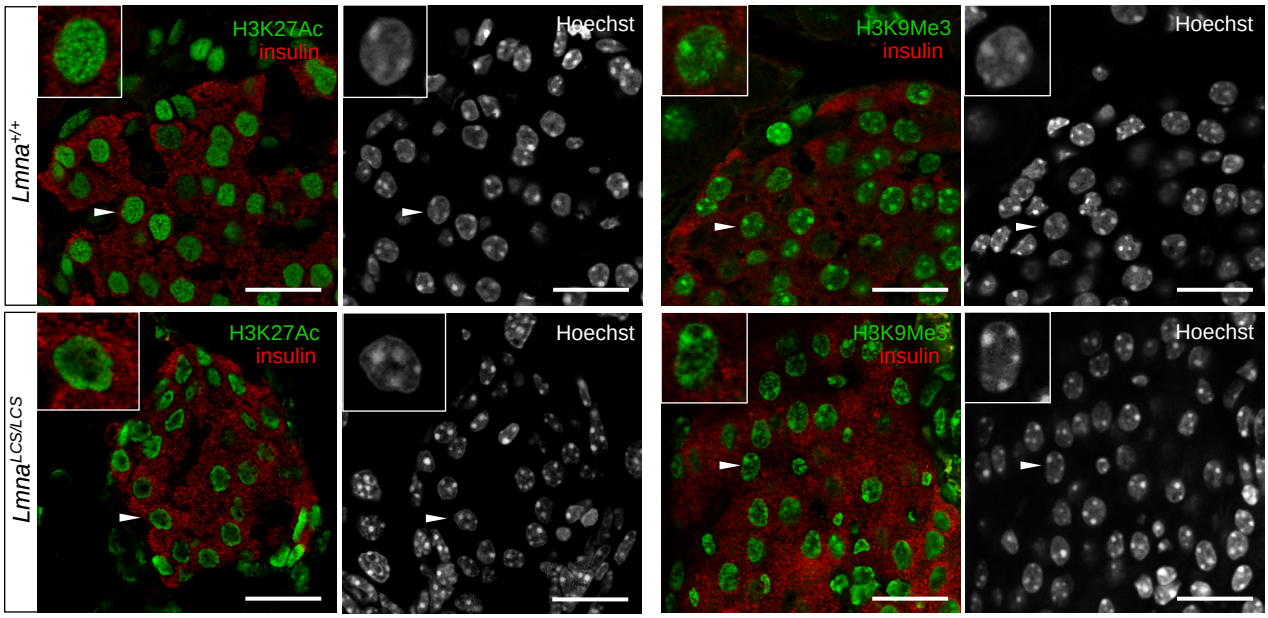

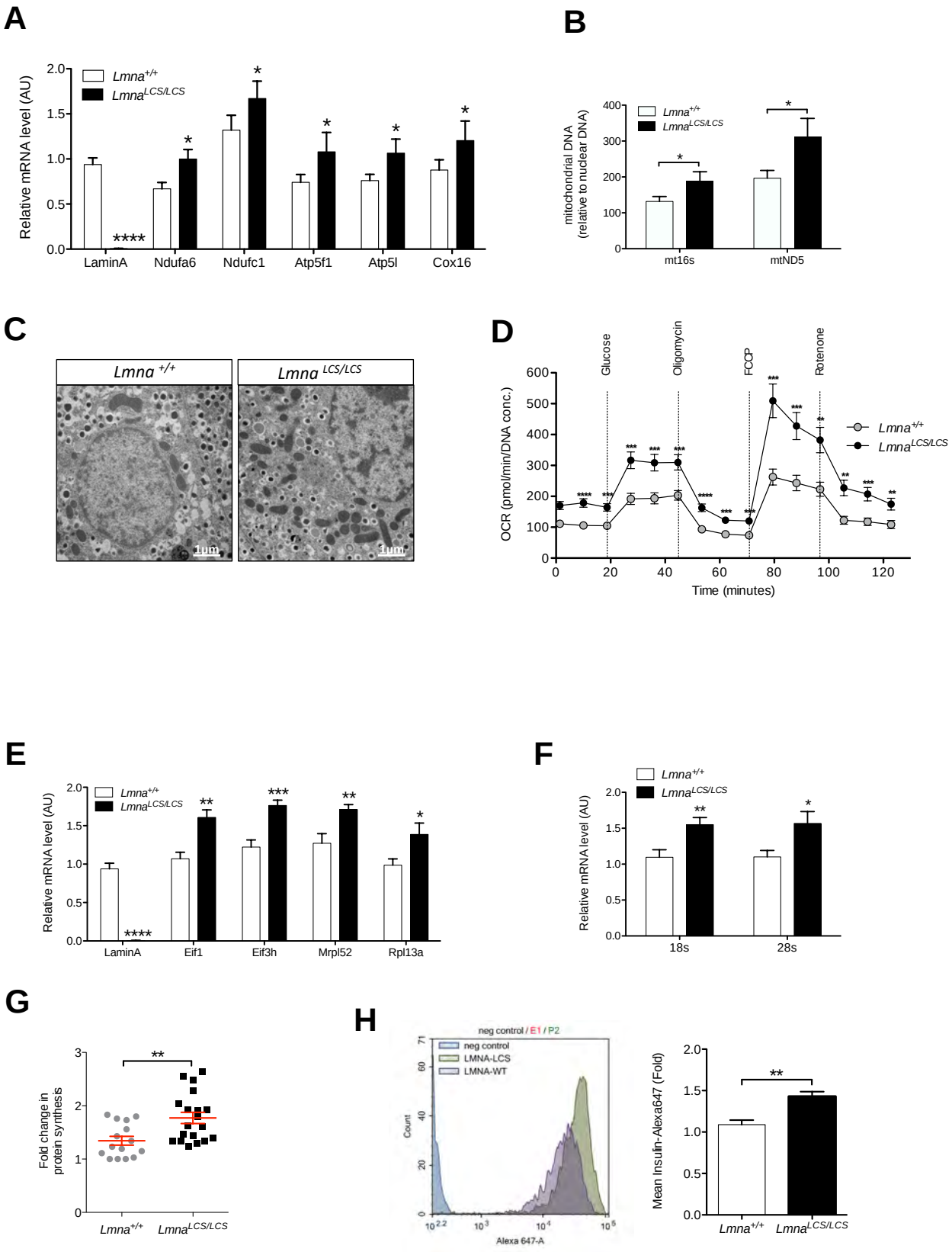
A
Relative mRNA level (AU)
Lmna+/+
LmnaLCS/LCS
LaminA
Ndufa6
Ndufc1
Atp5f1
Atp5l
Cox16
B
mitochondrial DNA (relative to nuclear DNA)
mt16s
mtND5
C
Lmna +/+
Lmna LCS/LCS
1µm
D
OCR (pmol/min/DNA conc.)
Glucose
Oligomycin
FCCP
Rotenone
Time (minutes)
E
Relative mRNA level (AU)
Eif1
Eif3h
Mrpl52
Rpl13a
F
18s
28s
G
Fold change in protein synthesis
H
neg control / E1 / P2
neg control
LMNA-LCS
LMNA-WT
Count
Alexa 647-A
Mean Insulin-Alexa647 (Fold)

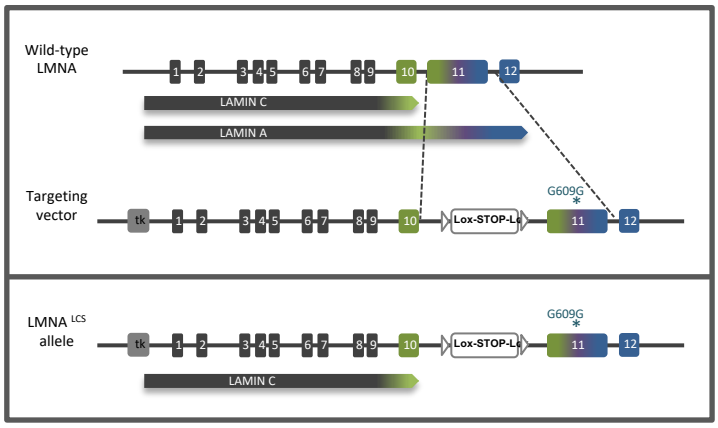

A) Structure of the targeted allele after homologous recombination. The "Lox-STOP-Lox" cassette insertion in intron 10 of LMNA gene induces the exclusive lamin C expression by promoting the use of lamin C polyadenylation site.

B) Expression of lamin A, lamin C and actin expression in the brain, liver, pancreas and muscle of 10-week-old *Lmna*$^{+/+}$ and *Lmna*$^{LCS/LCS}$ mice.

C) Representative HE staining images of pancreatic sections from 121-week-old *Lmna*$^{+/+}$ and 141-week-old *Lmna*$^{LCS/LCS}$ mice. The right image shows a magnification (4X) of the left image.

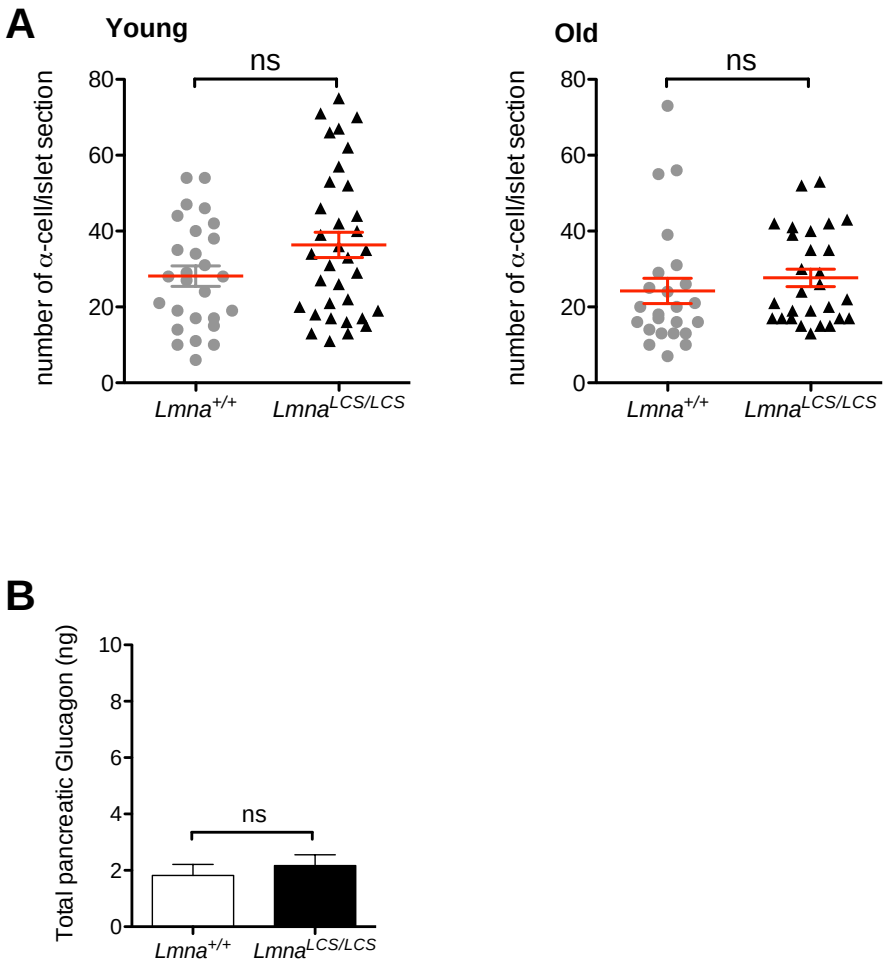

A) Quantification of number of α-cells per islet section in young vs old *Lmna*$^{+/+}$ and *Lmna*$^{LCS/LCS}$ mice (n=4 per group)

B) Glucagon content from total pancreata of old *Lmna*$^{+/+}$ and *Lmna*$^{LCS/LCS}$ mice (n=6 per group)

All values are expressed as the mean ± SEM. ns not significant by Student's unpaired t-test.

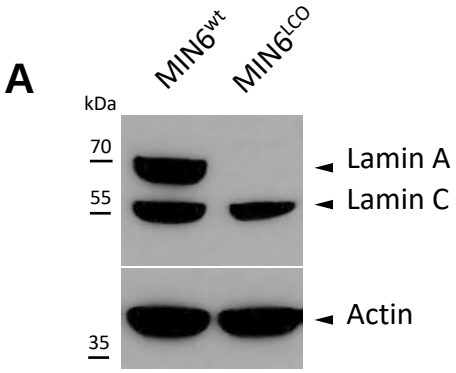

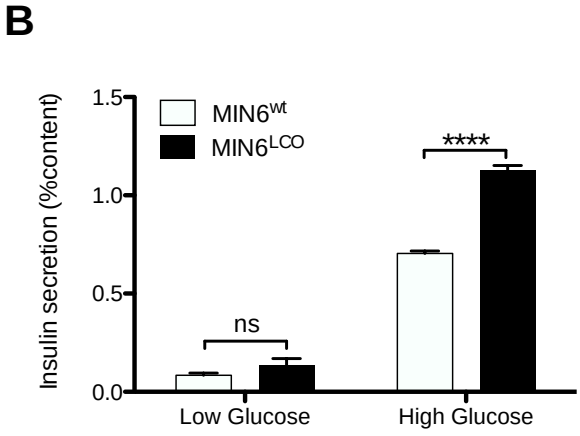

A) Lamin A and lamin C expression in CRISPR/Cas9-generated MIN6^{wt}, MIN6^{LCO} and MIN6^{LAO} cells as assessed by western blot.

B) GSIS in MIN6^{wt} and MIN6^{LCO} cells. The results were normalized to insulin content.

All values are expressed as the mean ± SEM. ****$p < 0.0001$ and ns not significant by Student's unpaired t-test.

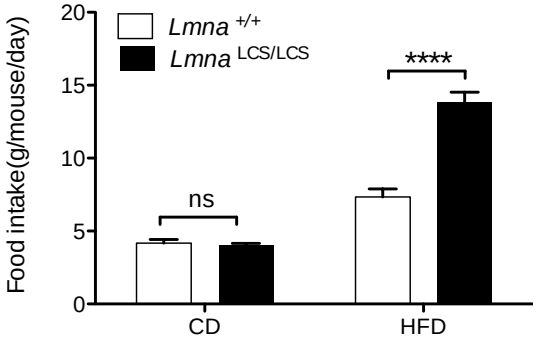

Mean food intake of CD or HFD in 30-week-old *Lmna*$^{+/+}$ and *Lmna*$^{LCS/LCS}$ mice (n=8 per group).

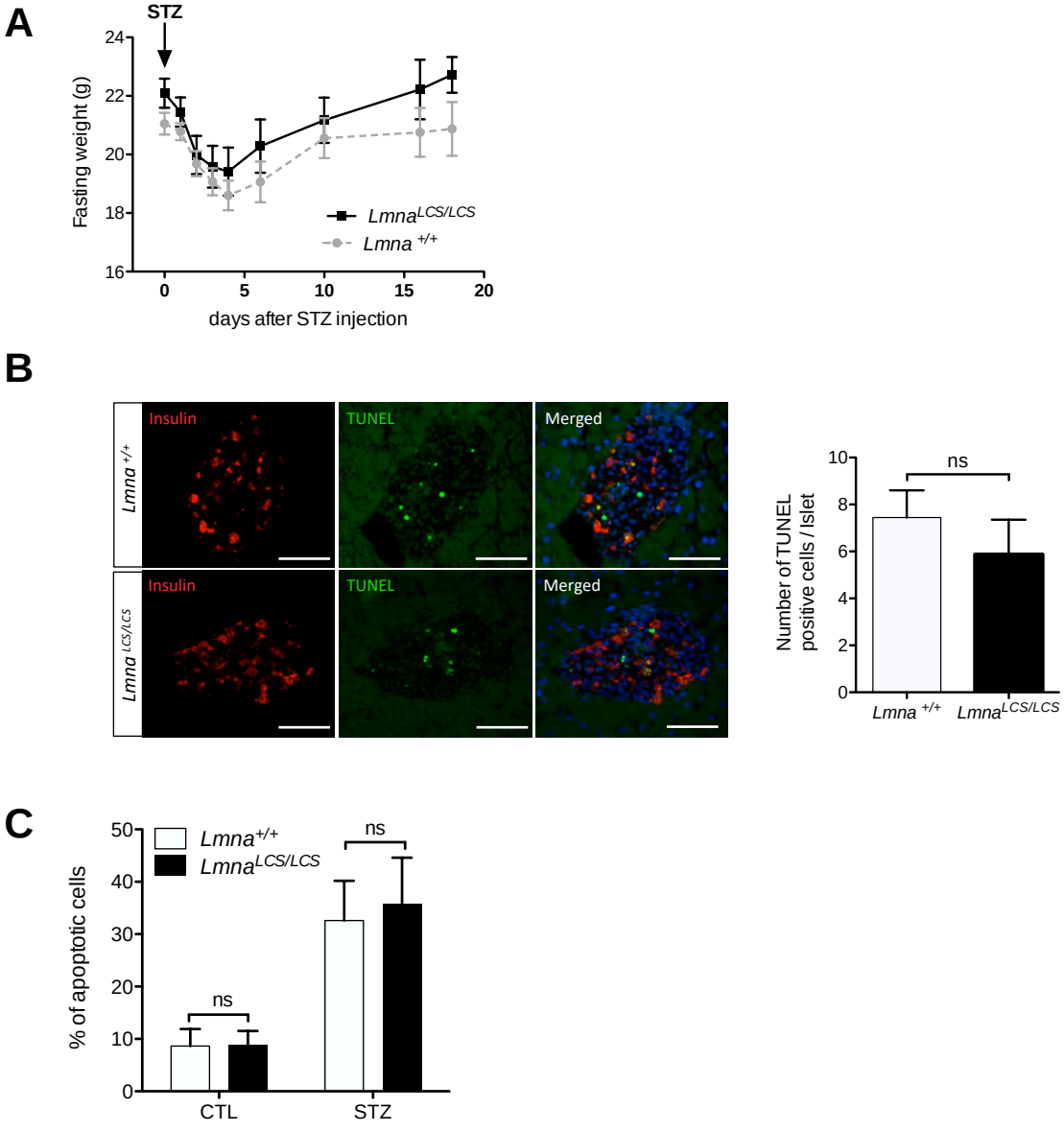

A) Body weight curve over time in *Lmna*$^{+/+}$ and *Lmna*$^{LCS/LCS}$ mice during STZ treatment (n=5 per group).

B) Representatives images (left panel) of TUNEL staining (green) on pancreatic sections from *Lmna*$^{+/+}$ and *Lmna* $^{LCS/LCS}$ mice obtained 48 h after STZ treatment (n=3 per group). Insulin is stained in red, and nuclei are stained with Hoechst (scale bar 50 µm). Quantification (right panel) of the number of TUNEL positive cells per islets.

C) FACS quantification of mean percentages of apoptotic MIN6^{wt} and MIN6^{LCO} cells treated with or without STZ (12 mM) for 5 h.

All values are expressed as the mean ± SEM. *$p<0.05$ and ns not significant by Student's unpaired t-test.

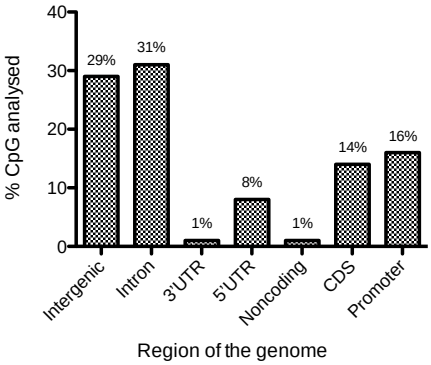

Distribution of the analyzed CpG sites in various regions of the genome.

Supplementary material

Western Blot

Mouse brain, liver, pancreas and muscle tissue samples were snap-frozen in liquid nitrogen immediately after collection. Samples were then reduced into powder form with a tissue grinder, homogenized and dissolved at 150 mg/ml in a buffer containing 63mM Tris-HCl (pH7.5), 2% (w/v) SDS, 5% (v/v) 2-mercaptoethanol and 8M urea. Samples were stored at -80°C. Protein extracts were size-fractionated on 4-12% gradient SDS-polyacrylamide Bis-Tris gels (ThermoFischer Scientific) and transferred to nitrocellulose membranes for Western blotting. Western blots were probed with a 1:1000 diluton of anti-lamin A/C (sc-20681-Santa Cruz Biotechnology, Santa Cruz, CA, USA), 1:4000 dilution of anti-Actin, clone C4 (#MAB1501 - Millipore, MA, USA).

Food intake

Food intake was measured three times a week over a period of one month with ten animals per genotype in individual cages.

Glucose-stimulated insulin secretion

For insulin secretion, 5 islets of 150–200µm diameter kept in 1,5ml microtubes were pre-incubated for 1 h at 37°C in Krebs–Ringer bicarbonate (KRB) buffer containing: 115mM NaCl, 4.7mM KCl, 6.2mM CaCl2, 20mM NaHCO3, 1.2mM MgSO4, 1.2mM KH2PO4, 16mM HEPES, 0.5% Free Faty Acid BSA, 10mM glucose. The pre-incubation medium was then replaced with KRB buffer supplemented with different glucose concentrations (Low: 3mM; High: 20mM). After incubation for 1 h at 37°C, the supernatant was collected and stored at -

80°C for later analysis of insulin content by ELISA (Mouse Ultrasensitive Insulin elisa-ALPCO, USA). Insulin content is collected after islets lysis in an Acid/Ethanol lysis buffer. Data are expressed as a ratio of insulin secreted/total insulin content.

For MIN6 GSIS assays, prior to glucose stimulation, cells were first starved in KRB buffer without glucose for 1h.

Total pancreatic insulin and glucagon content

Mouse pancreata were snap-frozen in liquid nitrogen immediately after collection. Samples were reduced into powder, resuspended in 2ml Acid/Ethanol lysis buffer and incubated O/N at 4°C. After sonication, samples were neutralized with 10% of 1M Na2CO3 and centrifuged. Total Insulin and Glucagon content were measured by ELISA (Mouse Ultrasensitive Insulin elisa-ALPCO, Mercodia Glucagon ELISA - 10 µL).

Flow cytometry

The islets were first dissociated into a free cell suspension with 0.05%Trypsine-0.5 mM EDTA. Cells were fixed with 1% PFA in PBS for 10 minutes, washed with PBS and permeabilised with 0.05% Triton X-100 for 10 minutes at 4°C. After blocking with PBS containing 1% BSA, 2% donkey serum, 50 mM glycine, and 0.5% gelatin, cell suspension was incubated with a guinea pig anti-insulin antibody (ab7842; Abcam) for 30 minutes at 4°C, washed and then reacted with a FITC-conjugated donkey anti-guinea pig antibody (F(ab')2 fragment; Jackson ImmunoResearch Labs). The cell suspension was then washed and analyzed by FACSCANTO II (Becton Dickinson).

MIN6 cell culture and apoptosis

The mouse insulinoma MIN6 pancreatic β-cell line (AddexBio) was maintained at 37°C in DMEM High Glucose, Glutamax, and sodium pyruvate (#31966-021, Thermo Fisher Scientific, MA, USA) supplemented with 15% fetal calf serum, 0.05 mM beta-mercaptoethanol and 100 µg/ml penicillin-streptomycin in an atmosphere of 95% air/5% CO_2.

To evaluate the MIN6-induced apoptosis, cells were treated with STZ (12 mM) before staining with Annexin-V-FITC (Invitrogen) and propidium iodide and then analyzed by flow cytometry (FACSCalibur, Becton Dickinson).

CRISPR-Cas9-mediated LCO MIN6 cell line

To generate the MIN^{LCO} cell line, we targeted exon 11 of the *Lmna* gene to enhance the use of the polyA site of lamin C located in intron 10. Gene-specific CRISPR sgRNA sequences were selected to generate a non-homologous end joining in exon 11 of the *Lmna* gene (gene ID: 4000) (Exon11-2119: 5'-ACTCGAAGCTTCCGCAGTGTGG-3').

The generated sgRNAs were inserted into the SIGMA pU6-gRNA. Both pU6-gRNA and pCMV-Cas9wt-2A-GFP or pCMV-Cas9 D10A-2A-GFP (SIGMA) were cotransfected into MIN6 cells using Lipofectamine 3000 Reagent (Thermo Fisher Scientific). GFP-positive cells were sorted by flow cytometry (FACSCalibur, Becton Dickinson), diluted, reseeded in 100 mm petri dishes and cultured for 2 weeks to obtain isolated clones. After handpicking clones for isolation, cells were collected and analyzed by western blot.

Histological studies

For paraffin treatment, pancreases were fixed with 4% paraformaldehyde, dehydrated, embedded in paraffin, sectioned (4µm), and stained with hematoxylin and eosin (HE) following standard procedures for morphological evaluation. HE staining of pancreatic sections was visualized with a Nanozoomer slide scanner (Hamamatsu). Scanned images were analyzed with NDP View software. The mean diameter of the Langerhans islets was determined by measuring the diameter of at least 150 islets per mouse (n=5) using NDP View software.

Immunohistochemistry and image acquisition

For immunohistochemistry, pancreas sections were deparaffinized, rehydrated, and incubated for antigen retrieval in citrate buffer at 95°C for 30 min. Nonspecific antibody binding was blocked by incubation with PBS containing 1%BSA, 0.05% Tween20 for 30 min at room temperature. Sections were then incubated in primary antibodies (see table 2) overnight at 4°C. After being washed, primary antibodies were detected using appropriate secondary antibodies. Nuclei were counterstained with Hoechst® 33342 (2µg/ml, ThermoFischer Scientific).

β-cell apoptosis after STZ treatment was determined using a Click-iT™ TUNEL Colorimetric IHC Detection Kit (#C10625, Thermofischer scientific)**.**

Widefield images were acquired using a Metamorph-driven (Molecular Devices, Sunnyvale, CA) Leica DM6000 fluorescence microscope with a 100X HCX Plan 0.7 - 1.4 NA oil objective (NA 1.32, Leica, Melville, NY) and a Coolsnap HQ2 camera (Photometrics, Woburn, MA). Confocal images were acquired using a Confocal Leica SP5-SMDmicroscope and a Leica 63×/1.4 oil HCX PL APO CS objective controlled using the Leica LAS AF software.

Ultrastructural transmission electron microscopy (TEM)

After isolation, 150 islets of Langerhans per mice and per genotype were immersed in a solution of 2.5% glutaraldehyde in Sorensen's buffer (0.1 M, pH 7.4) overnight at 4 °C. They were rinsed twice in Sorensen's buffer and post-fixed in a 0.5% osmic acid for 2 hours at room temperature in the dark. Tissues were dehydrated in a graded series of ethanol solutions (30-100%) and embedded in EmBed 812 with an Automated Microwave Tissue Processor for Electronic Microscopy, Leica EM AMW. Thin sections (70 nm; Leica-Reichert Ultracut E) of each block were collected at different levels. These sections were counterstained with uranyl acetate and observed on a Hitachi 7100 transmission electron microscope (TEM) in the Centre de Ressources en Imagerie Cellulaire de Montpellier (France).

RT-qPCR analysis

Total RNA was extracted from isolated islets using TRIzol (Life Technologies, USA). After precipitation in isopropanol, RNA pellets were washed in cold 75% ethanol and resuspended in nuclease-free water. Samples were quantified and evaluated for purity (260-nm/280-nm and 260-nm/230-nm ratio) with a NanoDrop ND-1000 spectrophotometer. Total RNA (1.5 µg) was then converted to cDNA with the Maxima First Strand cDNA Synthesis Kit (#K1642, Thermo Scientific, US). Gene expression was quantified by SYBR green real-time PCR on the LightCycler® 480 System (Roche Applied Science). Reactions were run in triplicate. The mean expression value for the housekeeping genes cyclophillin and TBP was used as an internal control to normalize variability in expression. Primer sequences are provided in Supplemental Table 1.

Mitochondrial DNA quantification

Isolated islets were digested 1h at 55 °C in a lysis buffer containing 100 mM Tris (pH 8), 5 mM EDTA, 0.2% SDS, 200 mM NaCl, and 0.1mg/ml proteinase K for DNA extraction. Quantitative PCR (qPCR) analysis of DNA samples diluted at 1 ng/µl was performed with primers specific for mitochondrial genes (*mtND5*, *mt16s*) and normalized to the mean of two nuclear genes (*LN11*, *HK2*). qPCR was performed with a LightCycler® 480 and LightCycler® 480 SYBR Green I Master (Roche).

RNA-Seq, RRBS, ATAC-Seq and Data analysis

RNA-Seq

RNA-Seq libraries construction

RNA-Seq libraries were constructed with the Truseq stranded mRNA sample preparation (Low throughput protocol) kit from Illumina. 400ng of total RNA were used for the construction of the libraries. Using poly-T oligo attached magnetic beads, total RNA was purified in order to obtain only poly-A mRNA. Following purification, the mRNA is fragmented into small pieces using divalent cations under elevated temperature. The cleaved RNA fragments are copied into first strand cDNA using SuperScript II reverse transcriptase, Actinomycin D and random hexamer primers. The Second strand cDNA was synthesized by replacing dTTP with dUTP. These cDNA fragments then have the addition of a single 'A' base and subsequent ligation of the adapter. The products are then purified and enriched with 15 cycles of PCR. The final cDNA libraries were validated with a Fragment Analyzer (Advanced Analytical, Ankeny, IA) and quantified using the Kapa Library quantification kit (Kapabiosystems). On 1 sequencing lane of a flowcell V4, and 1 sequencing lane of a flowcell V2, the 6 libraries were pooled in equal proportions, denatured with NaOH

and diluted to 16 pM before clustering. Cluster formation, primer hybridization and single-end read, 50 cycles sequencing were performed on cBot and HiSeq2500 (Illumina, San Diego, CA) respectively. Image analyses and base calling were performed using the Illumina HiSeq Control Software and the Real-Time Analysis component. Demultiplexing was performed using Illumina's conversion software (bcl2fastq 2.18). The quality of the raw data was assessed using FastQC from the Babraham Institute and the Illumina software SAV (Sequencing Analysis Viewer). Potential contaminants were monitored with the FastQ Screen software from the Babraham Institute.

RNA-Seq data analysis

We aligned RNA-seq reads to the mouse genome (UCSC mm9) with the splice junction mapper TopHat 2.1.1 (1), which used Bowtie 2.2.9 (2). We downloaded gene model annotations from the UCSC database (genes.gtf 31 August 2017) and GeneIDs from the NCBI (gene2refseq.gz, 31 August 2017). Final read alignments having more than 3 mismatches were discarded. We performed gene counting using the union mode of HTSeq-count 0.9.0 (3). Before statistical analysis, genes with less than 15 reads (cumulating all the analyzed samples) were filtered out. Counts were normalized using the Relative Log Expression (RLE) method as implemented in the Bioconductor (4) package edgeR 3.16.5 (5). Differentially expressed (DE) genes were identified using 3 different statistical methods: DESeq 1.26.0 (6), EdgeR, and DESeq2 1.14.1 (7). We corrected P-values for multiple testing using the Benjamini-Hochberg FDR method (8). Genes with adjusted P-value <0.05 were declared 'differentially expressed'. The final lists of DE genes were the genes common to the 3 tests. To perform the functional analysis of the resulting list of genes with the Gene Ontology (GO) annotations, the topGO(9) package from Bioconductor was used. Overrepresented GO terms

were identified using Fisher's exact test with the weight method that is implemented in the topGO package. As confidence threshold we used a P-value of 1%. To perform this analysis the differentially expressed genes were compared with those of all known genes present in the annotation. The GO categories were found in the Org.Mm.eg.db package based on the gene reporter EntrezGeneID.

Reduced Representation Bisulfite Sequencing

Libraries construction

Library construction was performed using the Premium RRBS kit (Diagenode). Briefly, for each sample, 100ng of intact genomic DNA were digested using MspI for 12 hours at 37°C. DNA ends were repaired and Diagenode indexed adaptors were ligated to each end of the repaired DNA. Each ligated DNA was quantify by qPCR using the Kapa Library quantification kit (Kapabiosystems) on a LightCycler 480 (Roche Life Science) prior to pooling (8 samples per pool). Each pool was submited to bisulfite conversion and desalted. Optimal PCR cycle number was determined by qPCR using the Kapa Library quantification kit (Kapabiosystems) before the final enrichment PCR. Once purified using magnetic beads (AMPure XP, Beckman Coulter), library pools were verified on Fragment Analyzer (AATI) and precisely quantified by qPCR using the Kapa Library quantification kit (Kapabiosystems). Each pool was denatured, diluted to a 18 pM concentration and spiked with a 10 % phiX Illumina's library before clustering. Clustering and sequencing were performed in paired end 2*50nt, 2 lanes per pool , according to the manufacturer's instructions on a Hiseq2500 using Rapid V2 clustering and SBS reagents.

Analysis of RRBS data

The sequencing quality control of RRBS data was identical to the one performed for RNA-Seq data. The un-methylated cytosine added at the end-repair step during library preparation was used as a built-in bisulfite conversion efficiency control. Sequences that contained the adapter on their 3' end were trimmed with cutadapt (https://cutadapt.readthedocs.org/en/stable/; minimaloverlap length between the read and the adapter of 5; discard trimmed reads shorter than 15). The option "--trimmed-only" was used to discard reads that did not contain the adapter. The percentage of non-bisulfite converted cytosines was then calculated as the number of times the filled in position at the 2nd base from the 3' end was not converted to T. Mean ± sd bisulfite conversion was 99.55 ± 0.03% for the read 1 and 99.63 ± 0.02% for the read 2 for the 24 samples.

Trim Galore (http://www.bioinformatics.babraham.ac.uk/projects/trim_galore/) was used to perform adapter trimming and quality control in two subsequent steps in order to remove the 2 additional bases that contained a cytosine which were artificially introduced at the end-repair step during the library preparation (--rrbs option). The mm9 mouse reference genome was prepared for Bismark 0.17.0 using bismark_genome_preparation script. Bismark software (version 0.17.0) from the Babraham Institute (10) was used to align trimmed RRBS reads to the mouse genome. Then, bismark_methylation_extractor extracted the methylation call for every single C analyzed.

Differential methylation analysis was performed using the methylSig (v0.4.4) Bioconductor R package (11). A site specific analysis was done for each CpG site covered by min 10 and max 500 reads using local information to improve variance estimation. A tiled analysis was also conducted by using the total number of cytosines in a windows of 25 bp. A cytosine or a region was declared differentially methylated if the adjusted p-value (according

to Benjamini-Hochberg multiple testing correction) was less than 0.05 and the difference of methylation percent above 25%.

Assay for Transposase-Accessible Chromatin (ATAC-Seq)

Cells were harvested and frozen in culture media containing 50% FCS, 40% RPMI and 10% DMSO. Cryopreserved cells were sent to Active Motif to perform the ATAC-seq assay. The cells were then thawed in a 37°C water bath, pelleted, washed with cold PBS, and tagmented as previously described (12), with some modifications based on (13). Briefly, cell pellets were resuspended in lysis buffer, pelleted, and tagmented using the enzyme and buffer provided in the Nextera Library Prep Kit (Illumina). Tagmented DNA was then purified using the MinElute PCR purification kit (Qiagen), amplified with 10 cycles of PCR, and purified using Agencourt AMPure SPRI beads (Beckman Coulter). Resulting material was quantified using the KAPA Library Quantification Kit for Illumina platforms (KAPA Biosystems), and sequenced with PE42 sequencing on the NextSeq 500 sequencer (Illumina).

Analysis of ATAC-seq data was very similar to the analysis of ChIP-Seq data. Reads were aligned using the BWA algorithm (mem mode; default settings). Duplicate reads were removed, only reads mapping as matched pairs and only uniquely mapped reads (mapping quality >= 1) were used for further analysis. Alignments were extended in silico at their 3'-ends to a length of 200 bp and assigned to 32-nt bins along the genome. The resulting histograms (genomic "signal maps") were stored in bigWig files. Peaks were identified using the MACS 2.1.0 algorithm at a cutoff of p-value 1e-7, without control file, and with the –nomodel option. Peaks that were on the ENCODE blacklist of known false ChIP-Seq peaks were removed. Signal maps and peak locations were used as input data to Active Motifs

proprietary analysis program, which creates Excel tables containing detailed information on sample comparison, peak metrics, peak locations and gene annotations.

For differential analysis, reads were counted in all merged peak regions (using Subread, v1.5.2), and the replicate groups for each condition were compared using DESeq2 (v1.24.0).

References

1. Kim D, Pertea G, Trapnell C, Pimentel H, Kelley R, Salzberg SL. TopHat2: accurate alignment of transcriptomes in the presence of insertions, deletions and gene fusions. Genome Biol [Internet]. 2013;14(4):R36. Available from: http://genomebiology.biomedcentral.com/articles/10.1186/gb-2013-14-4-r36
2. Langmead B, Salzberg SL. Fast gapped-read alignment with Bowtie 2. Nat Methods [Internet]. 2012 Apr 4;9(4):357–9. Available from: http://www.nature.com/articles/nmeth.1923
3. Anders S, Pyl PT, Huber W. HTSeq--a Python framework to work with high-throughput sequencing data. Bioinformatics [Internet]. 2015 Jan 15;31(2):166–9. Available from: https://academic.oup.com/bioinformatics/article-lookup/doi/10.1093/bioinformatics/btu638
4. Gentleman RC, Carey VJ, Bates DM, Bolstad B, Dettling M, Dudoit S, et al. Bioconductor: open software development for computational biology and bioinformatics. Genome Biol [Internet]. 2004;5(10):R80. Available from: http://www.ncbi.nlm.nih.gov/pubmed/15461798
5. Robinson MD, McCarthy DJ, Smyth GK. edgeR: a Bioconductor package for differential expression analysis of digital gene expression data. Bioinformatics [Internet]. 2010;26(1):139–40. Available from: http://www.ncbi.nlm.nih.gov/pubmed/19910308%5Cnhttp://www.pubmedcentral.nih.gov/articlerender.fcgi?artid=PMC2796818
6. Anders S, Huber W. Differential expression analysis for sequence count data. Genome Biol [Internet]. 2010;11(10):R106. Available from: http://genomebiology.biomedcentral.com/articles/10.1186/gb-2010-11-10-r106
7. Love MI, Huber W, Anders S. Moderated estimation of fold change and dispersion for RNA-seq data with DESeq2. Genome Biol [Internet]. 2014 Dec 5;15(12):550. Available from: http://genomebiology.biomedcentral.com/articles/10.1186/s13059-014-0550-8
8. Benjamini Y, Hochberg Y. Controlling the false discovery rate: a practical and powerful approach to multiple testing. J R Stat Soc [Internet]. 1995;57(1):289–300. Available from: http://www.jstor.org/stable/2346101%5Cnhttp://about.jstor.org/terms
9. Alexa, A R. TopGO: enrichment analysis for gene ontology. R Packag version 2(0). 2010;
10. Krueger F, Andrews SR. Bismark: a flexible aligner and methylation caller for Bisulfite-Seq applications. Bioinformatics [Internet]. 2011 Jun 1;27(11):1571–2. Available from: https://academic.oup.com/bioinformatics/article-lookup/doi/10.1093/bioinformatics/btr167
11. Park Y, Figueroa ME, Rozek LS, Sartor MA. MethylSig: a whole genome DNA methylation analysis pipeline. Bioinformatics [Internet]. 2014;30(17):2414–22. Available from: http://www.ncbi.nlm.nih.gov/pubmed/24836530%5Cnhttp://www.pubmedcentral.nih.gov/articlerender.fcgi?artid=PMC4147891
12. Buenrostro JD, Giresi PG, Zaba LC, Chang HY, Greenleaf WJ. Transposition of native chromatin for fast and sensitive epigenomic profiling of open chromatin, DNA-binding proteins and nucleosome position. Nat Methods. 2013;10(12):1213–8.
13. Corces MR, Trevino AE, Hamilton EG, Greenside PG, Sinnott-Armstrong NA, Vesuna S, et al. An improved ATAC-seq protocol reduces background and enables interrogation of frozen tissues. Nat Methods. 2017;14(10):959–62.

RT qPCR primers	
Cyclophillin Fw	5'-GTT GGC CAG GCT GGT GTC CAG-3'
Cyclophillin Rev	5'-CTG TGA TGA GCT GCT CAG GGT GG-3'
TBP Fw	5'-GGT GGC GGG TAT CTG CTG GC-3'
TBP Rev	5'-TGG GGA GGC CAA GCC CTG AG-3'
Mm Ndufa6 Fw	5'-GAA TGC CCA TGT CAC AGA-3'
Mm Ndufa6 Rev	5'-AAA CCG CAT AAC GTG TGT-3'
mNdufc1 Fw	5'-TTC CTC TGG ATT CAC CCT CA-3'
Ndufc1 Rev	5'-CAT GAG GAG CGC GAG TAT TT-3'
Mm Atp5f1 Fw	5'-CTG GCC TTG GAG GTC ACT TA-3'
Mm Atp5f1 Rev	5'-ATG CAC TTG GCA ATG GTC-3'
Mm Atp5l Fw	5'-AGC TGT GCT GAA TGG TTT-3'
Mm Atp5l Rev	5'-TAG CCA ACA ATG CCA CGT-3'
Mm Cox16 Fw	5'-GCG CTG AGT CTA CAA CTT-3'
Mm Cox16 Rev	5'-ACC AGC AAC AAC ATG GGA-3'
Mm Eif1 Fw	5'-ACA GAG AAA CGG CAG GAA-3'
Mm Eif1 Rev	5'-CTG GTC ACC CTG TAG CTG AA-3'
Mm Eif3h Fw	5'-TGG CGG ATA AGC ACG AAT-3'
Mm Eif3h Rev	5'-CGA CGC TGC TGA TAC TGA-3'
Mm Mrpl52 Fw	5'-GGA GAA GCT TGC AAG ACG-3'
Mm Mrpl52 Rev	5'-TGA TTC GGA AGT GGG CTT CT-3'
Mm Rpl13a Fw	5'-ATG GGA TCC CTC CAC CCT-3'
Mm Rpl13a Rev	5'-CAG CCG AAC AAC CTT GAG-3'
28S Fw	5'-TAG CAG CCG ACT TAG AAC -3'
28S Rev	5'-CTC CCA CTT ATT CTA CAC-3'
18S Fw	5'-GGA GCC TGA GAA ACG GC-3'
18S Rev	5'-GGG TCG GGA GTG GGT AAT TTT-3'

Mitochondrial DNA	
mND5Fw	5'-GGC AGA CGA ACA AGA CAT CCG-3'
mND5Rev	5'-GCT AGG CGT TTG ATT GGG TT-3'
m16s Fw	5'-CCG CAA GGG AAA GAT GAA AGA-3'
m16s Rev	5'-TCG TTT GGT TTC GGG GTT TC-3'
LN11 Fw	5'-TGG CAG GCA GCT TGG TAG TC-3'
LN11 Rev	5'-AAT GGC TGG GAC AGA GCA GC-3'
mHK2Fw	5'-GCC AGC CTC TCC TGA TTT TAG-3'
mHK2Rev	5'-GGG AAC ACA AAA GAC CTC TTC-3'

Supplemental table 1 : List of primers for real-time PCR

Antibody	Reference	Dilution	Company
Rabbit anti-Phospho-histone H3 Ser10	#06-570	1/200	Merck Millipore
Guinea pig anti-insulin	#06-570	1/100	AbCam
Mouse anti-Glucagon clone K79bB10	#G2654	1/200	Sigma
Mouse anti-somatostatin YC7	#MA5-16987	1/100	ThermoFischer
Rabbit anti-H3K27Ac	Ab-4729	1/400	AbCam
Rabbit anti-H3K9Me3	Ab-8898	1/400	AbCam
Fluorescein-DBA (Dolichos biflorus Agglutinin)	#MA5-16987	1/200	Vector Laboratories
Goat anti-guinea pig IgG Alexa647	#MA5-16987	1/200	ThermoFischer
Goat anti-mouse IgG Alexa488	#MA5-16987	1/200	ThermoFischer
Goat anti-mouse IgG Alexa555	#MA5-16987	1/200	ThermoFischer
Goat anti-rabbit IgG Alexa555	#MA5-16987	1/200	ThermoFischer
Click-iT™ TUNEL Colorimetric IHC Detection Kit	#MA5-16987		ThermoFischer
FITC-conjugated donkey anti-guinea pig antibody	706-095-148	1/100	Jackson ImmunoResearch Labs

Supplemental table 2 : List of antibodies